A stochastic model for protein localization in Caulobacter crescentus bacterium

An Do,[a] Blerta Shtylla[b,c]

[a]Institute of Mathematical Sciences, Claremont Graduate University, Claremont, CA, USA; [b]Mathematics Department, Pomona College, Claremont, CA, USA; [c]Current Address: Early Clinical Development, Pfizer Worldwide Research, Development, and Medical, Pfizer Inc., San Diego, CA 92121

ABSTRACT

Caulobacter crescentus bacterial cells use a minimal three component Par partition system to segregate DNA during asymmetric division. Precise division plane placement is tightly controlled by MipZ protein gradients that are thought to interact with Par proteins. How these complex protein interactions generate precise measurements in the face of stochastic fluctuations is of significant interest. Here, we first developed a detailed computational model used to study key interactions between Par and MipZ proteins that control chromosome segregation. In addition, we developed a minimal intermittent-search model that captured key ParB/ParA interactions in support of chromosome copy movement. Lastly, we found the competition between ParA and MipZ proteins for ParB complex binding sites to be sufficient in order to generate experimentally observed MipZ bipolar gradients. Our models provide a framework to study how the movement of the DNA copy could communicate with the division site placement proteins in *Caulobacter crescentus* cells.

1 Introduction

During cell division, chromosome segregation is facilitated by a minimal Par family of ATPases in *Caulobacter crescentus* (*C. crescentus*) bacteria. The ParABS partition system consists of ParA, a deviant Walker-type ATPase and ParB, a protein that forms a complex by binding to *parS* DNA sites (Surovtsev et al., 2016; Thanbichler and Shapiro, 2008; Mohl and Gober, 1997; Toro et al., 2008; Figge et al., 2004). During the DNA replication process, a chromosome-associated ParB complex interacts with a ParA dimer cloud that starts at the new pole and extends to the old pole, where ParB copies are first located prior to chromosome copy segregation (Easter Jr and Gober, 2002; Figge et al., 2004). It is believed that the dynamic interactions between the chromosome-associated ParB complex and the ParA cloud are responsible for the observed directed movement of the bacterial chromosome copy from the old to the new pole (Toro et al., 2008; Ptacin et al., 2010; Shebelut et al., 2010). Besides ParA and ParB, the polar landmark protein PopZ, which localizes both in the cytoplasm and also forms a polar scaffold (Lim et al., 2014; Ptacin et al., 2014; Bowman et al., 2008) is thought to play an important role in the division mechanics of *C. crescentus*. PopZ has been implicated in a variety of processes during DNA replication and segregation, such as: 1) maintaining the ParA gradient concentration (Bowman et al., 2008; Ebersbach et al., 2008; Bowman et al., 2010; Ptacin et al., 2014), 2) recruiting proteins to the poles (Bowman et al., 2008, 2010; Ebersbach et al., 2008) and 3) anchoring the duplicated ParB/ParS complex at the poles (Bowman et al., 2008; Ebersbach et al., 2008).

Shortly after chromosome segregation is complete, FtsZ, a tubulin-like GTPase polymerizes and forms a ring-like structure that is found to assemble approximately near the middle of the cell corresponding to the division plane. The localization of FtsZ ring components seems to be influenced by its interactions with another ATPase called MipZ (Mid-cell positioning of FtsZ), which in turn forms bipolar gradient that peaks at each pole (Bowman et al., 2008; Sundararajan and Goley, 2017). FtsZ assembles into a ring structure in regions of low MipZ dimer concentration (Quardokus and Brun, 2002). It is interesting to note that the MipZ gradient is slightly asymmetric with the minimum shifted toward the new cell pole, in line with the a similar bias in the positioning of FtsZ ring (Ptacin et al., 2010; Schofield et al., 2010; Kiekebusch and Thanbichler, 2014). The slight bias in positioning of the FtsZ ring is important, as this bacterium undergoes asymmetric division with one stalked daughter cell destined to undergo additional division and the other a swarmer cell. MipZ protein localization is thought to be controlled

by its interactions with ParB/ParS complex and DNA (Thanbichler and Shapiro, 2006; Kiekebusch et al., 2012). Even though MipZ is the only known spatial regulator of FtsZ localization in *C. crescentus* (Sundararajan and Goley, 2017), it is not clear how MipZ interactions with the ParAB partition machinery can precisely control FtsZ ring localization that facilitates asymmetric cell division (Kiekebusch and Thanbichler, 2014).

While many details about ParB and ParA reactions in *Caulobacter crescentus* are becoming elucidated, how their interactions generate persistent directed movement of ParB complexes from the old to the new pole is still not clear. To this end, several mathematical models have been put forward to understand ParB complex movement. The first generation of models (Banigan et al., 2011; Shtylla and Keener, 2012) were developed assuming that ParA monomers formed continuous filaments across the cell length, similar to spindles in eukaryotic cells, based on data from the experiments of Ptacin et al. (2010). The key underlying idea of ParB complex movement in this initial modeling setup was that multiple weak contacts between ParB and ParA filament disassembly were sufficient to allow ParB to track a shrinking ParA fiber bundle to the new pole. A more general setup of a burnt-bridge Brownian ratchet model that examined hydrolysis-dependent movement of ParB on a ParA track was explored by Shtylla and Keener (2015).

Since then, evidence against ParA polymers has emerged (Hwang et al., 2013; Vecchiarelli et al., 2012, 2014; Li et al., 2016, 2009), instead supporting a setup where ParA dimers occupy an unstructured cloud on the nucleoid. A second generation of computational models that relies on a reaction-diffusion mechanism does not evoke ParA depolymerization but rather depends on the two main properties of ParA/ParB system: elastic ParB binding to nucleoid ParA, and ATP hydrolysis effects on ParA dimers due its association with a ParB complex (Hu et al., 2015, 2017; Lim et al., 2014; Surovtsev et al., 2016). In the model proposed by Hu et al. (2015, 2017) diffusion is a major mechanism for ParB motility; whereas in the 'DNA-relay model' described by Lim et al. (2014) and by Surovtsev et al. (2016) ParB complexes move due to the pull of multiple elastic connections with DNA-bound ParA. Either model does not explicitly consider the role of polar PopZ in ParA accumulations as well as the ATP cycle of ParA dimerization.

The connection between the Par system and MipZ accumulations has not been explored as much as the ParA dynamics from the modeling stand point. Shtylla (2017) examined a mean field PDE model that included the interactions between Par and MipZ proteins. However, PDE formulations rely on high protein numbers and *C. crescentus* has only a few hundred Par proteins. The stochastic fluctuations in protein numbers and their localization can be of tremendous significance in the context of precise MipZ polar gradient organization and has not been explored before to our knowledge.

In this work, the core question we wanted to examine was how dynamic Par machinery protein localization could be connected with and possibly modulate MipZ accumulations at the single cell level. First, we proposed a detailed computational reaction-diffusion model that assembled all the reactions of key divisional proteins such as ParA, ParB, PopZ and MipZ and tracked all protein reactions and individual protein localizations within a bacterial cell. Although the computational model results were in qualitative agreement with relevant experimental studies, the implicated reaction network is complex and computationally intensive to simulate and to explore in depth. Additionally, we necessarily needed to include some parameters whose precise values were unknown due to lack of experimental measurements, which introduced uncertainty in model predictions. Thus, to better understand and capture the range of model responses, we performed a systematic sensitivity analysis (local and global) of parameters in order to identify critical parameters that affect ParB complex movement and MipZ accumulations. Relying upon insights provided from the computational model results, as well as ranking of critical parameters from sensitivity analysis, we were able to develop a minimal PDE model in the random intermittent search framework that captured the most salient features of ParB/ParA interactions. This minimal model is novel as random intermittent search strategies (reviewed by Bénichou et al., 2011) have not been applied before in the context of protein localization in bacterial cells. The minimal model helped us shed light into mechanisms controlling ParB movement for different parameter regimes that were in agreement with the computational modeling approach.

Since the computational reaction-diffusion model could handle low protein numbers, we used it to simulate MipZ bipolar gradients at the single cell level and then examined how robust MipZ gradients could be in constraining Z-rings at the the experimentally observed positions. We found that uncertainty in Z-ring positioning can be significant when MipZ protein levels are low, thus we conjecture that additional mechanisms for division plane placement might be at play in these cells.

2   Materials and Methods

2.1   Computational model reactions

We develop a computational model that incorporates interactions between ParA, ParB, polar PopZ scaffolds, and MipZ in a three dimensional rectangular cell, diagrammed in Figure 1(A-B). The following set of reactions and assumptions are used to derive the model.

(A)

| Nucleoid | Direction of duplicated ParB |

(B)

Old Pole — New Pole

half cell height

cell width — cell length

● ParA dimer ✦ ParA monomers ● MipZ dimer ✦ MipZ monomers
● PopZ matrix ● Immobilized ParB ● Mobilized ParB

(C)

ParA reactions

$$AM + AM \underset{k_5}{\overset{k_1}{\rightleftharpoons}} ADc$$

$$ADc \xrightarrow{k_2} ADn$$

$$B + ADn \xrightarrow{k_3} B.ADn$$

$$B.ADn \xrightarrow{k_4} B + 2AM$$

$$ADp \xrightarrow{k_2} ADn$$

PopZ reactions

$$Zm + 2AM \xrightarrow{k_6} AM.Zm.AM$$

$$AM.Zm.AM \xrightarrow{k_8} Zm + ADp$$

$$Zm + B \xrightarrow{k_{15}} B.Zm$$

MipZ reactions

$$MM + MM \underset{k_{14}}{\overset{k_9}{\rightleftharpoons}} MDn$$

$$MM + MM \underset{k_{13}, B}{\overset{k_{11}, B}{\rightleftharpoons}} MDn$$

Figure 1: *C. crescentus* diagram and corresponding model reactions. (A) Schematic model of partitioning (Par) system in *C. crescentus*. (B) 3D rectangular model represents half of the cell. The bottom surface, where ParA and MipZ nucleoid dimers co-locate, represents an idealized mid-plane nucleoid region and the two end faces represent two reactive old and new polar regions. ParA (orange) bind to the nucleoid DNA and get released into cytoplasm as monomers due to ParB(green) hydrolysis. ParA is also sequestered by PopZ matrix(purple) each polar region. MipZ(blue) monomers can bind to ParB and convert into dimers that bind the nucleoid DNA. MipZ dimerization is slower without ParB. (C) Corresponding chemical reactions among ParA monomers (AM), cytoplasmic ParA dimer (ADc), nucleoid bound ParA dimers (ADn), polar nucleoid-binding ParA dimers (ADp), ParB complex (B), MipZ monomers (MM), nucleoid bound MipZ dimers (MDn), PopZ (Zm) included in our model, ParA-PopZ complex (AM.Zm.AM), ParB-ParA complex (B.ADn), ParB-PopZ complex (B.Zm). The values of these reaction rates are listed in Table 1. No flux condition is implemented for all boundaries.

ParA reactions.   ParA is an ATPase that interacts with DNA and co-localizes with the bacterial nucleoid (Vecchiarelli et al., 2010; Ptacin et al., 2010; Vecchiarelli et al., 2012; Hwang et al., 2013). ParA undergoes a slow multi-step conformational transition upon binding of ATP (Vecchiarelli et al., 2010) and then dimerizes in the cytoplasm (Ptacin et al., 2010; Vecchiarelli et al., 2010). ParA dimers are competent to bind non-specifically to nucleoid DNA (Vecchiarelli et al., 2010; Hwang et al., 2013). ATP turn-over by ParA is slow and is coupled to ParA detachment from the nucleoid in monomer form (Vecchiarelli et al., 2010). Correspondingly, in our model ParA proteins can exist in cytoplasmic monomer form (AM) and cytoplasmic and nucleoid-bound dimer form (ADc and ADn) where ADc denotes cytoplasmic ParA dimer and ADn denotes nucleoid-bound ParA dimer. In the interest of simplicity, we omit the ATP-binding steps of ParA monomers prior to dimerization in our model. The kinetic schemes corresponding to ParA dimerization cycles are illustrated in Figure 1(B).

ParB reactions.   ParB proteins form a dense complex in the centromere-like *parS* region of the DNA (Mohl and Gober, 1997; Mohl, Easter, and Gober, Mohl et al.; Toro et al., 2008). Upon DNA replication two ParB complexes originate proximal to the cell stalk (old pole): one copy remains anchored at the old pole whereas the newly replicated chromosome ParB complex translocates to the other end of the cell (new pole) following the retracting edge of a cloud of ParA (Ptacin et al., 2010; Schofield et al., 2010). The ParB complex is thought to be a primary mediator of chromosome segregation through simultaneous binding and removal of ParA from DNA (Ptacin et al., 2010; Vecchiarelli et al., 2010; Schofield et al., 2010). Specifically, ParB stimulates ATP hydrolysis of ParA dimers, thus causing their break down into monomeric form and release from the nucleoid (Ptacin et al., 2010; Vecchiarelli et al., 2010; Schofield et al., 2010; Hwang et al., 2013). In accordance, in our model we allow multiple ParA dimers to interact with two ParB complexes and undergo a hydrolysis reaction, detailed in the kinetic scheme in Figure 1(C).

Polar PopZ reactions.   PopZ proteins localize at both cell poles, where they form a polymeric network, or matrix that serves to anchor multiple division proteins including ParB complexes through direct binding (Bowman et al., 2008; Ptacin et al., 2010; Schofield et al., 2010; Laloux and Jacobs-Wagner, 2013; Ptacin et al., 2014). At the initial stages of chromosome replication PopZ releases the new ParB complex copy from the old pole and generates two focal matrices at each pole (Laloux and Jacobs-Wagner, 2013; Ptacin et al., 2014). Polar PopZ matrices have been shown to have a critical role in the polar recruitment of ParA released during ParB/ParA interactions (Ptacin et al., 2014). In addition, the polar landmark protein TipN that is implicated in the recruitment of new pole markers such as the flagellum, is found at the new pole where it has been shown to directly bind ParA monomers (Schofield et al., 2010). The enhanced interactions between ParA, PopZ, and TipN at the new pole are thought to create a condensed ParA accumulation there, thus creating a ParA gradient (Schofield et al., 2010; Ptacin et al., 2010, 2014). We incorporate these effects in our model by including binding between free ParA monomers and two distinct polar matrices (Zm) located at the two cell poles, thus creating polar ParA monomer complexes (AM.Zm.AM), illustrated in Figure 1. In addition, we allow for dimerization of ParA into a nucleoid binding competent form (ADp) within the polar matrix, in agreement with the idea that matrix capture of ParA monomers favors their re-dimerization and release into the cytoplasm (Ptacin et al., 2014). In our model we do not explicitly include TipN, instead we include its role by varying the total number of generic PopZ proteins at each pole in order to capture differences in polar accumulation between the old and new pole. Thus, a mutant cell Δ*tipN* is implemented as a scenario in which both poles contain the same number of PopZ proteins in our model.

MipZ reactions.   The protein MipZ is another important *C. crescentus* division ATPase that localizes dynamically in coordination with Par proteins (Thanbichler and Shapiro, 2006; Kiekebusch et al., 2012). MipZ can exist in both monomer form (MM), cytoplasmic dimer (MDc) and nucleoid-bound form (MDn) (Thanbichler and Shapiro, 2006; Kiekebusch et al., 2012). Similar to ParA, MipZ binds non-specifically to the nucleoid in an ATP dependent fashion, whereby ATP-bound MipZ dimers associate with DNA and MipZ monomers are released in the cytoplasm upon slow hydrolysis of ATP. MipZ initially accumulates at the old pole and then displays a moving front that coincides with ParB complex movement to the new pole, subsequently resulting in a bipolar accumulation of MipZ that accumulates around the two ParB complexes at each pole. In contrast to ParA, MipZ dimers have an inefficient dimerization rate on their own but in the presence of ParB, MipZ's dimerization is strongly favored (Kiekebusch et al., 2012). Correspondingly, in our model ParB complexes can capture multiple MipZ monomers, which then dimerize and are thus competent to bind the nucleoid, illustrated in Figure 1(B)-(C). Finally, MipZ monomers can also slowly dimerize and bind the nucleoid independently of ParB.

2.2   Stochastic simulation of the model reactions

Spatial reaction simulation algorithm.   We implemented simulations that incorporated all the model reactions in a three-dimensional rectangular cell, as illustrated in Figure 1(B) and in Supplementary Material, Table S1. A rectangular domain was chosen because it was the simplest framework for implementation of boundary conditions and surface reactions. With this approach we were able to capture key surface reactions at the cell poles corresponding to rectangular faces as well as movement along the long axis of the cell. We implemented reaction simulations using an efficient particle-based software called Smoldyn

(version 2.4.7) (Andrews, 2016) that uses an accurate off-lattice method to simulate reaction-diffusion networks on arbitrary domains and surfaces. This software produces reliable results in agreement with analytical predictions (Andrews et al., 2010) and has been used in various particle based simulations in cell biology, with several applications to the related *E. coli* Min system (Lipkow et al., 2005). Code scripts used to generate model results are given in the Supplementary Material, Section 5.

We outline the key features of the spatial reaction simulator algorithm. Each protein in our reaction network is treated as a point-like particle that diffuses in three dimensional space with continuous position variables and continuous time. There are two key ingredients to take care of in this setting: 1) diffusion of molecules in a closed domain, 2) reactions between molecules and molecules and surfaces.

Diffusion. Particle diffusion is simulated using a *Brownian dynamics* approach in which displacement for a diffusing particle in one time step Δt is obtained by drawing a random displacement along x,y and z-coordinates from the Gaussian distribution $(G_B(\cdot))$ that arises as the solutions for diffusion equation of the probability density function of finding a molecule at some point in space and time. Specifically, the probability of moving a particle a random displacement Δr, (where $r = (x, y, z)$) at each time step, namely $p_B(r + \Delta r, t + \Delta t)$ is the product of the Gaussian distribution $(G_B(\cdot))$ along x,y and z coordinates

$$p_B(\mathbf{r} + \Delta \mathbf{r}, t + \Delta t) = G_B(\Delta x) G_B(\Delta y) G_B(\Delta z)$$

$$G_B(\Delta x) = \frac{1}{2\sqrt{\pi D_B}} \cdot \frac{1}{\sqrt{\Delta t} \exp\left(-\frac{\Delta x^2}{2s^2}\right)}$$

where $\Delta x, \Delta y, \Delta y$ are the Cartesian displacements, $G_B(\Delta x)$ is normalized Gaussian with mean 0 and standard deviation *s*.

Reactions. In this framework, a diffusion-limited bimolecular reaction $A + B \rightarrow C$ occurs once two molecules A and B are separated by a binding radius (σ_b). For reversible reactions such as $A + B \leftrightarrow C$, to avoid a nearly instantaneous reaction back to C, the A and B dissociation products are initially separated by a fixed distance, namely the unbinding radius (σ_u) which is larger than binding radius. Both radii are derived from the reaction rate for this physical description as discussed in (Andrews and Bray, 2004; Andrews et al., 2010). We note here that this approach only addresses bi-molecular reactions; in our model all reactions are decomposed into multiple bi-molecular interactions when more than two particles interact. Where necessary, BioNetGen (Blinov et al., 2004) was used along with Smoldyn to automatically and accurately decompose multi-molecular reactions.

All the reactions are executed during each time step Δt, which is calculated internally by the algorithm. The need to track individual molecules in this setting imposes high computational demands and thus efficient algorithm implementation and reproducibility are of paramount importance. Therefore, we implemented our model in a robust and replicable framework; detailed discussion of algorithms implemented in Smoldyn can be found in (Andrews and Bray, 2004; Andrews, 2016; Andrews et al., 2010).

Model setup. Reactions were simulated within a model cell represented by a 3D rectangular cube with default dimensions of 3 µm in length, 0.3 µm in width and 0.7 µm in height, Figure 1(B). Two cube end surfaces (left and right) represent two reactive polar regions on which PopZ can experience two-dimensional surface diffusion. If ParA and ParB are within the binding radius of polar PopZ, they will be converted into polar complexes that diffuse on the polar surfaces (see reactions from Figure 1C). These reactive cube end surfaces serve as PopZ matrices in our model, i.e. we do not explicitly simulate three dimensional PopZ matrix dynamics. The bottom surface is where ParB, ParA and MipZ nucleoid bound dimers diffuse on and interact with all other proteins that are in its proximity. We implemented no flux boundary conditions on all cell boundaries so that total protein numbers were conserved in the cell. Unless otherwise stated, we simulate reactions between 300 ParA monomers, 900 MipZ monomers, 1 PopZ monomer at the old pole and 5 PopZ at the new pole (Shtylla, 2017; Lim et al., 2014). At the start of each simulation, one ParB complex copy is held fixed at the old pole while the duplicated ParB complex can freely move inside the rectangular domain, ParA and MipZ monomers were initially distributed uniformly within the cell. The main computational bottleneck arises from ParB complexes, which can interact with both multiple ParA and MipZ molecules, in addition to anchoring on the polar PopZ matrix. This creates a combinatorial challenge when accounting for all bi-molecular reactions. In accordance, we limited the total number of ParB complex binding sites to four in total (note that these sites are available to ParA dimers *and* MipZ dimers). Even in this simplified setup, there is high computational load due to the high number of possible ParB complex states inside the cell. To resolve this, we employed the BioNetGen package (Blinov et al., 2004) that can automate the generation of complex reaction networks prior to execution with Smoldyn. We developed custom Matlab scripts to process and analyze the results from the spatial simulator.

ParA/MipZ monomers and cytoplasmic dimers can diffuse freely inside the rectangular model cell. In *C. crescentus*, the nucleoid contains DNA and it occupies most of the interior cell volume. In our model, we do not model DNA dynamics, instead, we assume that the entire volume of the cell is occupied by nucleoid. In practice, this means any species inside our model cell can convert into nucleoid-bound species with some prescribed rate.
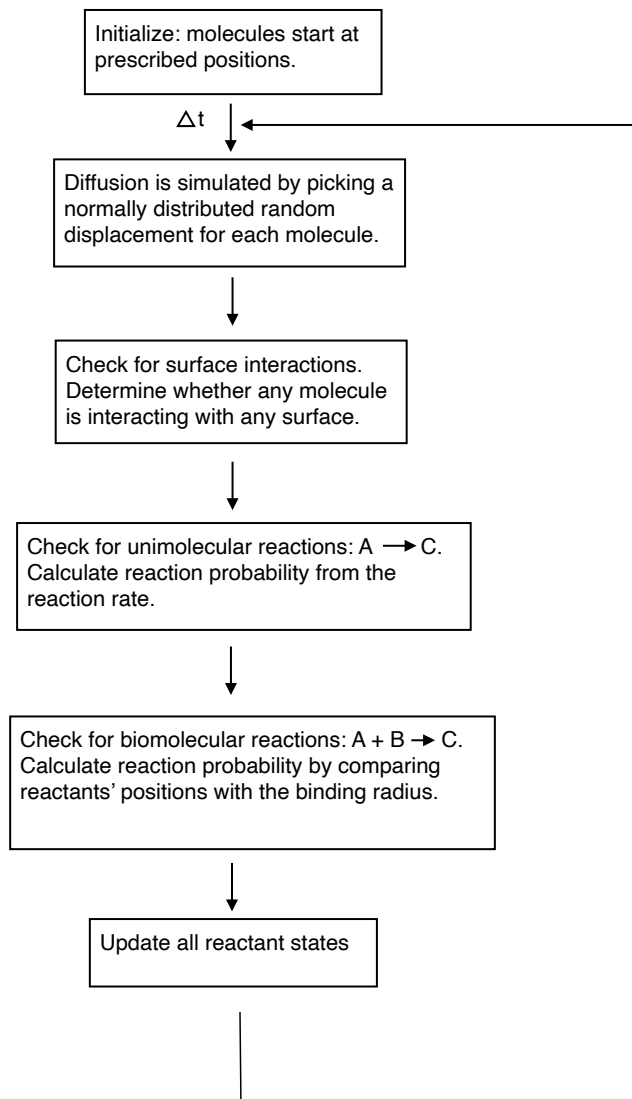
Figure 2: Flowchart of the spatial reaction simulator adapted from Andrews et al. (2010). Smoldyn algorithm treats each molecule in the reaction network as point-like particle. At each time step, diffusion is first simulated by randomly picking a random displacement for each molecule. Surface interactions are then determined if the molecules interact with any surface at each time step. The probability for the unimolecular reactions to occur is computed from the reaction rates. Lastly, the probability of the bimolecular reactions is computed by comparing the positions between the two reactants with the binding radius. The time step Δt is calculated as detailed by Andrews and Bray (2004).

With the above assumptions, we can simulate a full three dimensional model (sample code provided in the Supplementary Material). The model was initialized with one ParB held fixed at the old pole, a free ParB, 300 cytoplasmic ParA monomers, 1 PopZ at the old pole and 5 PopZ on the new pole. We observed ParA monomers being recruited by the polar PopZ matrices and forming cloud of ParA dimers near both poles. However, due to the asymmetric distribution of PopZ between the poles, more ParA dimers were found near new pole. Although mobile ParB could freely move inside the cell, it moved in a directed fashion toward the new pole with small variation along the z-axis; effectively moving along two dimensional surface. Once close to the new pole, ParB anchored at the new pole by interacting with PopZ there.

Two-dimensional ParB path reduction.   Full three dimensional cell model simulations generate a significant amount of protein position data with small variation along the z-axis during segregation of the ParB complex from the old to the new pole. However, experimental tracking data of ParB segregation from the new to the old pole that we used to calibrate the model are given at most in two dimensions along a cross section of the bacterial cell. In light of this and in order to simplify the simulations and data analysis, we reduced model complexity by constraining ParB complex movement to the bottom the cell box. This assumption allows us to analyze the ParB complex movement on a planar axis with no z-coordinate variation. In this setting, ParB diffuses on the bottom surface and interacts with all inner cell binding partners that are in its proximity. In addition in this set up, ParA and MipZ dimers once converted to nucleoid bound species can bind to the bottom surface. Comparison studies did not show significant changes in the segregation movement of the complex from one pole to the other using this reduction as opposed to a full three dimensional simulation. Therefore for the remainder of this paper we chose to retain this planar constraint setup for ParB, as illustrated in Figure 1(B). The values of the implemented reaction rates are listed in Table 1.

3   Results

3.1   Computational model results

We first ran a few control cases to make sure that there were no artifacts introduced in the simulations. Specifically, we simulated our model with only two ParB complexes (no ParA/MipZ/PopZ). The model results showed that no movement bias emerged and that ParB experienced pure diffusion when partner proteins were missing. Details on these simulations are given in Supplementary Material, Figures S1–S3.

ParB displays directed movement in the presence of both ParA gradient and PopZ.   Next, we simulated a cell that had asymmetric accumulation of PopZ at the poles. For these simulations we included 1 PopZ at the old pole, 5 PopZ at the new pole, 300 ParA monomers initially uniformly placed across the cell, 1 ParB was anchored at the old pole while the other ParB was initially positioned in proximity to the old pole. All parameter values for Par reactions correspond to the baseline values in Table 1.

In Figure 3(A)-(B) we show typical ParB trajectories along both the cell length and cell width, as well as a kymograph illustrating the position of ParA dimers in relation to ParB in Figure 3(C). In order to track the interactions between ParB and ParA, we recorded ParB's binding state to ParA. In Figure 3(A)-(B) blue trajectory corresponds to ParB when it is not bound to any ParA dimers and red corresponds to ParB when it is bound to at least one ParA dimer. Our results show that long runs correspond with ParB binding to at least one ParA dimer while short runs correspond with ParB not bound to any ParA. Additionally, ParB shows directed movement toward the new pole by trailing the edge of a shrinking ParA gradient, in agreement with data, as illustrated in Figure 3(C). Our results also demonstrate that ParA proteins in turn form a gradient that peaks at the new pole due to higher PopZ presence at the new pole versus the old pole (5 PopZ at the new pole and 1 PopZ at the old pole.)

We recorded ParB's position along the cell length only (x-axis) and then smoothened the data using a Fast Fourier Transform (FFT). Run length was calculated in micrometers (μm) as the length of the path for which ParB did not reverse direction. Run time (in minutes) was defined as the duration corresponding to each run length and run speed was computed in μm/min as the ratio of run length to run time. For our purposes, a run length is considered to be short if it is less than 0.1 μm, otherwise, it is called a long run length. Therefore, instead of manually assigning 'slow' and 'fast' phases as in (Lim et al., 2014), we categorize using our threshold for a 'slow' phase with a short run length and a 'fast' phase with a long run length.

In Figure 3(D)-(F) we ran the run length analysis for 100 independent simulations, and observed that average run lengths and run speeds increase due to ParB complex experiencing directed motion toward the new pole in the presence of ParA gradient. We computed an average ParB run speed of about 4 μm/min, which is faster than the reported speed in (Lim et al., 2014); note however that our run length and run time estimates are different than those in (Lim et al., 2014), so it is likely that this is affecting estimates of run speeds. Later we will show that ParB complex run speeds can be controlled by varying a few important model parameters.

Table 1: Model Parameters. Parameters are obtained by varying their values within their range of uncertainty until the simulated data are in agreement with available experimental data.

Parameter	Notation	Model range	Baseline	Reference range	Reference
Rate of ParA dimerization	k_1	$0.5 \times 10^{-5} \, \mu\text{m}^3\text{s}^{-1}$	$0.000005 \, \mu\text{m}^3\text{s}^{-1}$	$0.011 \, \mu\text{m}^3\text{s}^{-1}$	Vecchiarelli et al., 2010
ParA nucleoid binding rate	k_2	$0.001 - 0.01 \, \text{s}^{-1}$	$0.01 \, \text{s}^{-1}$	$0 - 0.01 \, \text{s}^{-1}$	Hu et al., 2017; Lim et al., 2014
ParA-ParB association rate	k_3	$0.1 - 3300 \, \text{s}^{-1}$	$3000 \, \text{s}^{-1}$	$10^3 - 10^6 \, \text{s}^{-1}$	Hu et al., 2015; Vecchiarelli et al., 2014
Rate of ParB-induced ParA dimer hydrolysis	k_4	$0.01 - 5 \, \text{s}^{-1}$	$0.5 \, \text{s}^{-1}$	$0.5 - 3 \, \text{s}^{-1}$	Surovtsev et al., 2016; Hu et al., 2015, 2017
ParA natural hydrolysis rate	k_5	$0.0004 - 0.05 \, \text{s}^{-1}$	$0.008 \, \text{s}^{-1}$	$0.0004 - 0.05 \, \text{s}^{-1}$	Hu et al., 2017
ParA-PopZ polar sequesting rate	k_6	$0.001 - 0.01 \, \text{s}^{-1}$	$0.9 \, \text{s}^{-1}$	$0.01 - 1.67 \, \text{s}^{-1}$	Shtylla and Keener, 2015
ParA polar flux rate	k_7	$0.001 - 1 \, \text{s}^{-1}$	$0.01 \, \text{s}^{-1}$	$0.01 - 1.67 \, \text{s}^{-1}$	Bonny et al., 2013; Shtylla and Keener, 2015
ParA polar to cytoplasmic conversion rate	k_8	$0.001 - 1 \, \mu\text{m}^3\text{s}^{-1}$	$0.45 \, \mu\text{m}^3\text{s}^{-1}$	$0.01 - 1.67 \, \text{s}^{-1}$	Bonny et al., 2013; Shtylla and Keener, 2015
MipZ natural dimerization rate	k_9^*	$0.0004 - 0.05 \, \text{s}^{-1}$	$0.01 \, \text{s}^{-1}$		Ranges chosen to match with k_5
ParB-MipZ monomer reaction rate	k_{11}^*	$0.001 - 0.01 \, \text{s}^{-1}$	$0.01 \, \text{s}^{-1}$		Ranges chosen to match with k_6
MipZ dimerization rate (with ParB)	k_{13}	$0.0001 - 3 \, \text{s}^{-1}$	$0.2 \, \text{s}^{-1}$	$0.0001 - 3 \, \text{s}^{-1}$	Shtylla, 2017
MipZ natural hydrolysis rate	k_{14}	$0.0001 - 0.01 \, \text{s}^{-1}$	$0.001 \, \text{s}^{-1}$	$0.0001 - 0.01 \, \text{s}^{-1}$	Kiekebusch et al., 2012
ParB-PopZ reaction rate	k_{15}^*	$0.001 - 0.01 \, \text{s}^{-1}$	$0.001 \, \text{s}^{-1}$		Ranges chosen to match with k_6
Diffusion coefficient of free ParA/MipZ monomers	$D_{MM} = D_{AM}$	$10^{-2} - 10^{-1} \, \mu\text{m}^2\text{s}^{-1}$	$0.02 \, \mu\text{m}^3\text{s}^{-1}$	$10^{-2} - 10^{-1} \, \mu\text{m}^2\text{s}^{-1}$	Shtylla, 2017; Elowitz et al., 1999; Weber et al., 2010
Diffusion of DNA-bound ParA dimer	D_{ADn}	$10^{-4} - 10^{-2} \, \mu\text{m}^2\text{s}^{-1}$	$0.01 \, \mu\text{m}^2\text{s}^{-1}$	$10^{-4} - 10^{-2} \, \mu\text{m}^2\text{s}^{-1}$	Lim et al., 2014; Surovtsev et al., 2016; Hu et al., 2017, 2015
Diffusion coefficient of MipZ dimer	D_{MDn}	$10^{-4} - 10^{-2} \, \mu\text{m}^2\text{s}^{-1}$	$0.001 \, \mu\text{m}^3\text{s}^{-1}$	$10^{-4} - 10^{-2} \, \mu\text{m}^2\text{s}^{-1}$	estimated same as D_{ADn}
Diffusion coefficient of PopZ	D_{Zm}	$10^{-2} - 10^{-1} \, \mu\text{m}^2\text{s}^{-1}$	$0.01 \, \mu\text{m}^3\text{s}^{-1}$	$10^{-2} - 10^{-1} \, \mu\text{m}^2\text{s}^{-1}$	estimated same as D_{ADn}
Diffusion coefficient of ParB	D_B	$0.0001 - 0.1 \, \mu\text{m}^2\text{s}^{-1}$	$0.0001 \, \mu\text{m}^2\text{s}^{-1}$	$0.0001 - 0.1 \, \mu\text{m}^2\text{s}^{-1}$	Hu et al., 2015; Sliusarenko et al., 2011; Hu et al., 2017; Laloux and Jacobs-Wagner, 2014
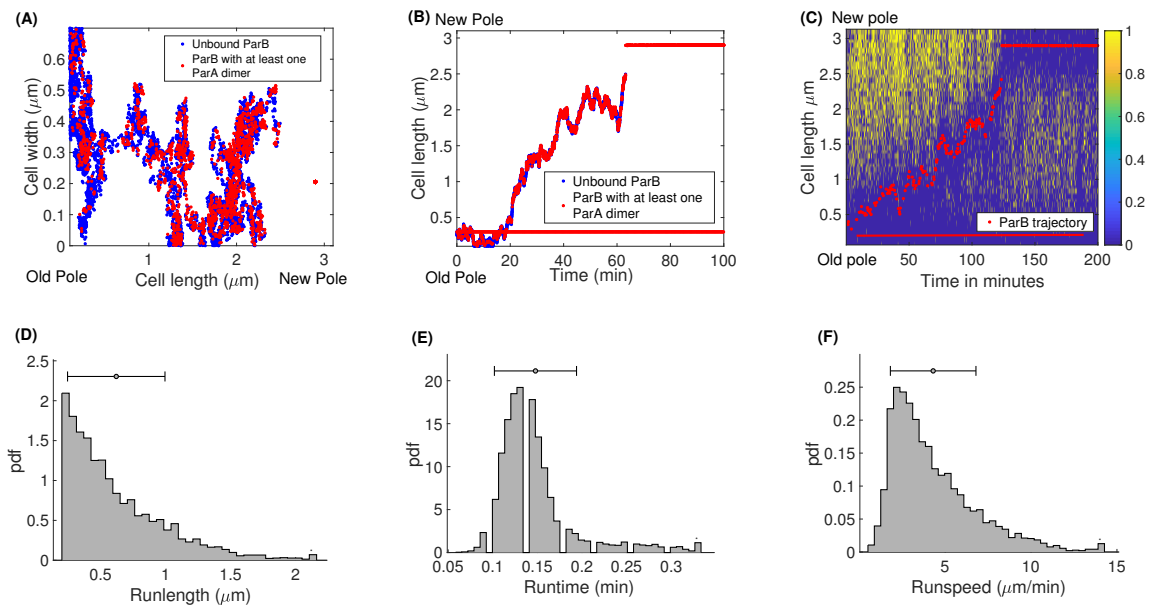
Figure 3: ParB motion using model baseline parameter values. (A) A representative 2D trajectory of ParB position along the nucleoid for 100 minutes of simulation. (B) A representative trajectory of both immobile ParB (old pole) and free ParB along the cell for 100 minutes of simulation; blue marker corresponds to unbound ParB and red marker corresponds to the ParB associated with at least one ParA dimer. (C) A kymograph of ParA distribution (yellow) overlaid with ParB's trajectory (red) for 100 minutes of simulation. (D)-(F) Histograms of ParB complex runlength, runtime and run speed ($n = 100$).

ParB movement reversals in response to ParA overproduction.　Since ParB shows sensitivity to ParA gradient, next, we sought to test how ParB segregation changed when ParA was overproduced in the cell and thus likely to lose new pole directed gradient, in accordance with the experiments of Schofield et al. (2010). Specifically, Schofield et al. (2010) proposed that polar saturation with ParA in cases of over-expression could cause oscillatory ParB movement that tracked the edge of a moving ParA gradient from one pole to the other. To capture these scenarios in our model, we tripled the number of ParA monomers in the cell to 900 ParA monomers, while PopZ matrix was altered gradually as follows: a) no PopZ at the two poles to represent PopZ being fully saturated with ParA and unable to sequester any more ParA, b) equal ratio of PopZ at the two poles (1 PopZ proteins per pole) to capture polar saturation in conditions of symmetrical capacity for binding ParA (i.e., a ParA over-expression in ΔTipN mutant) c) PopZ ratio of 1 to 2 between old and new pole (1 PopZ at the old pole and 2 PopZ at the new pole) to represent a ParA over-expression in a wild-type cell where there is a mild non-symmetrical binding capacity for ParA due to the action of TipN at the new pole.

　　Figure 4 shows model simulation results for the three scenarios listed above. We observed that a ParA cloud fails to condense at the new pole when ParA is over-expressed both in the case when there is either no PopZ around or equal amount of PopZ in each pole, as seen in Figure 4(A)-(B). This created a lack of new-pole directed gradient and correspondingly lack of directed ParB movement. Overabundant ParA also formed large clouds expanding from the new pole toward the old pole causing ParB to stochastically transition between poleward and anti-poleward motion due to equal ParA presence both close to the old pole and the new pole. However, when introducing slight asymmetry in PopZ between the 2 poles, the ParA cloud was able to form a weak gradient from the new pole to the old pole, and ParB in this case (Figure 4C) experiences directed movement. Note that overexpressing ParA created trailing ParA behind ParB which caused frequent ParB reversals and delayed segregation even when there was more PopZ at the new pole compared to the old, Figure 4(C). Yet, in all test cases, we did not observe sustained oscillatory waves of ParA and correspondingly ParB between the two poles, which were sometimes observed in (Schofield et al., 2010). Oscillatory (pole to pole traveling waves) could emerge if there is a delay between the ParB reading of ParA gradient changes, however, in our model the ParB complex instantaneously senses any change in local ParA gradient cues which prevents it from experiencing pole to pole tracking of ParA waves. Oscillatory waves were shown to emerge when an additional ParA sensing species is added in the mix to add delay to ParB gradient reading as outlined by Shtylla (2017).

ParB-meditated ATP hydrolysis of ParA plays a critical role in complex movement directionality.　Thus far our model results indicate that ParB directionality is critically affected by the presence of ParA gradient that peak at the new pole. However, in the computational model of Lim et al. (2014), it was intriguingly reported that ParB complexes failed to produce
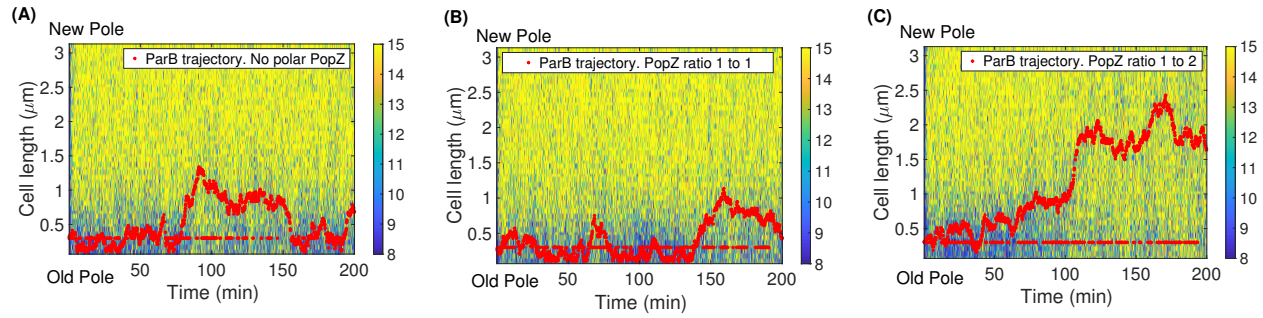
Figure 4: ParB motion under ParA overexpression and polar saturation. (A) ParA kymograph overlaid with ParB trajectories and no PopZ at two poles to capture polar PopZ is fully saturated with ParA and unable to bind with additional ParA. (B) Same as (A) but with 1 PopZ at each pole to capture polar PopZ saturation with ParA but still able to have a symmetric capacity for binding ParA. (C) Same as (A) but with 1 PopZ at the old pole and 2 PopZ at the new pole to capture a mild polar saturation but with asymmetrical binding capacity for ParA between the 2 poles. There are 900 ParA for all simulations, all other parameters are set to baseline Table 1.
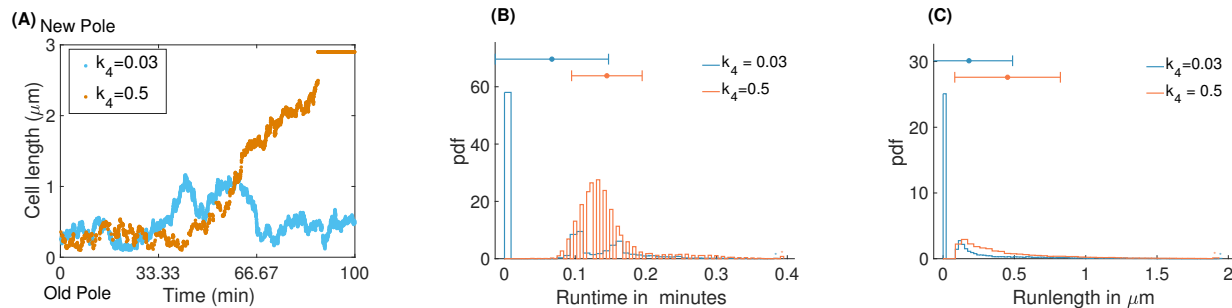
Figure 5: Comparison of ParB motion using different values of k_4 . All parameters are kept at the baseline values. (A) 2D trajectory of ParB in both the long and short cell axes, blue marker represents ParB's trajectory using $k_4 = 0.03 \text{ s}^{-1}$(Lim et al., 2014) and orange marker represents ParB's trajectory using $k_4 = 0.5 \text{ s}^{-1}$. (B) Distribution of ParB run time corresponding with $k_4 = 0.03 \text{ s}^{-1}$ (blue) and $k_4 = 0.5 \text{ s}^{-1}$ (orange). (C) Distribution of ParB run length corresponding with $k_4 = 0.03 \text{ s}^{-1}$ (blue) and $k_4 = 0.5 \text{ s}^{-1}$ (orange).

directed movement *in the presence* new-pole-directed ParA gradient. We thus next examined conditions for which Lim et al. (2014) simulated their model in our own computational model. For this purpose we simulated the model with parameter values that follow Lim et al. (2014) when applicable such as we adjusted the rate ParB-induced ParA dimer hydrolysis down to $k_4 = 0.03 \text{ s}^{-1}$; otherwise parameters were kept at the baseline values from Table 1. In Figure 5(A) we compared our model results with slow k_4 (mimicking Lim et al., 2014) by tracking the ParB trajectory along the cell. In Figure 5(A) light orange marker represents our baseline value of k_4 and light blue marker represents the lower k_4 of Lim et al. (2014). In addition in Figure 5(B)-(C) we calculated the average run length, run time and run speed of ParB in both cases ($n = 100$).

Our simulations in Figure 5(A) show that when the rate ParB-induced ParA dimer's hydrolysis was lowered to $k_4 = 0.03 \text{ s}^{-1}$ in our model, ParB took a long time to hydrolyze one ParA dimer (33 seconds) and thus experienced diffusive movement even though a ParA gradient was present due to asymmetric distribution of PopZ between the two poles (2 PopZ monomers at the old pole and 4 PopZ monomers at the new pole); this agrees with the observed diffusive motion of ParB of Lim et al. (2014) due to the low rate $k_4 = 0.03 \text{ s}^{-1}$ which effectively dilutes the effects of the ParA gradient on ParB motion. When changing the rate ParB-induced ParA dimer hydrolysis to our baseline of $k_4 = 0.5 \text{ s}^{-1}$, ParB could hydrolyze one ParA dimer quickly (2 seconds) and thus experienced directed movement trailing a ParA gradient and anchored at the new pole (orange marker trajectory in Figure 5(A)). These results indicate that ParB is likely to fail to produce directed movement in (Lim et al., 2014) due to the low ParB-induced hydrolysis rate of ParA in presence of ParB (k_4). On the other hand, it must be remarked that ParB's diffusion coefficient in (Lim et al., 2014) has also been considered to be too slow to admit directed ParB movement (Hu et al., 2015, 2017). Overall, our model results indicate that the hydrolysis rate k_4 can have a critical role in the ability of the ParB complex to move in agreement with data, and thus model parameter ranges should be carefully and systematically studied when considering ParB motility regimes. We investigate the effects of parameter variation on ParB movement statistics in the next section.
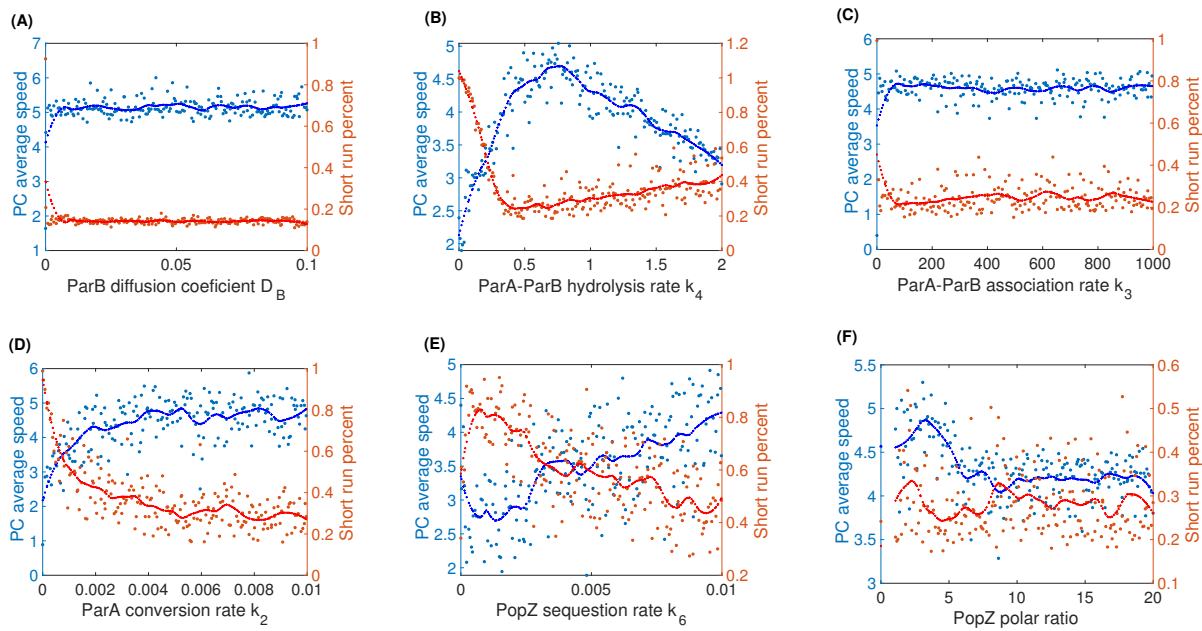
Figure 6: ParB average speed (left blue y-axis) and short-run percentage (right red y-axis) as a function of a single parameter while the rest are kept at the baseline values. Solid red and blue lines mark LOESS fitting. (A) Relationship between ParB average speed and short-run percentage with D_B. (B) Relationship between ParB average speed and short-run percentage with k_4. (C) Relationship with Relationship between ParB average speed and short-run percentage with k_2. (D) Relationship between ParB average speed and short-run percentage with k_2. (E) Relationship between ParB average speed and short-run percentage with k_6. (F) Relationship between ParB average speed and short-run percentage with ratio of PopZ proteins at the new pole and the number of PopZ proteins at the old pole (PopZ polar ratio).

3.1.1 Parameter sensitivity analysis

Local sensitivity analysis.   As a first step, we performed single parameter variation studies, i.e., we varied one parameter within the reported ranges we could find in the literature, while keeping the rest of the parameters at their baseline values. We calculated two metrics of model output for each parameter input. First, we computed the partition complex' *average directed speed* as it translocated from one pole to another. Average directed speed is defined here as the mean of the run speeds ($n = 100$) corresponding to run lengths that are longer than 0.1 μm, i.e. long-runs. Secondly, we computed the *percentage of partition complex' short-runs* defined as the percent of run lengths that are shorter than 0.1 μm, i.e., short-runs. The percentage short-runs are the ratio between the short run length to the total run lengths calculated over $n = 100$ simulations as described in the previous section.

Selected results from single parameter variation calculations are shown in Figure 6. To summarize, k_4, k_2, k_6 showed interesting trends in the model behavior indicating a critical role of ParB-induced hydrolysis rates and ParA gradient formation in determining the ability of the ParB complex to experience directed movement. Specifically, our results are in support of an optimal range of the rate ParB-induced ParA-ATP hydrolysis, k_4 values for which ParB attains its highest speed and correspondingly lowest percent of slow runs. On the other hand, as ParA nucleoid binding rate k_2 increased, the ParB speed also increased until it saturated to a constant value, indicating high sensitivity of ParB movement to ParA binding to the nucleoid. Similarly, ParB velocities increased with the rate of ParA sequestration at the pole, k_6 and the PopZ polar ratio, which in turn strengthen the effect of an asymmetric ParA gradient in the cell. The rest of the parameters show fast saturation of velocities and percent slow runs in the tested ranges indicating that their effect might not be as significant past a particular low threshold. To probe these relationships a bit more closely, we investigated model behavior in the cases where two parameters were varied simultaneously, as shown in Figure 7.

The two parameter heat maps in Figure 7 show the dependence of the partition complex mean velocity and percent slow runs between ParA nucleoid binding rate k_2 and ParB-induced ParA-ATP hydrolysis rate, k_4 and ParA polar sequestration rate, k_6. We note the complementary nature of the mean velocity and percent slow run results showcased by the heatmaps; this indicates that high velocities indeed correspond to directed movement, whereas low velocities correspond to non-directed or diffusive movement as marked by a high percentage of slow runs. We also remark that two parameter regimes emerge in the heatmaps, corresponding to directed (high velocity) and diffusive (non-directed movement). Specifically, in Figure 7(A)-(B), ParB experienced directed movement in the optimal k_4 ranges, with the optimal range widening as k_2 increased. This indicates
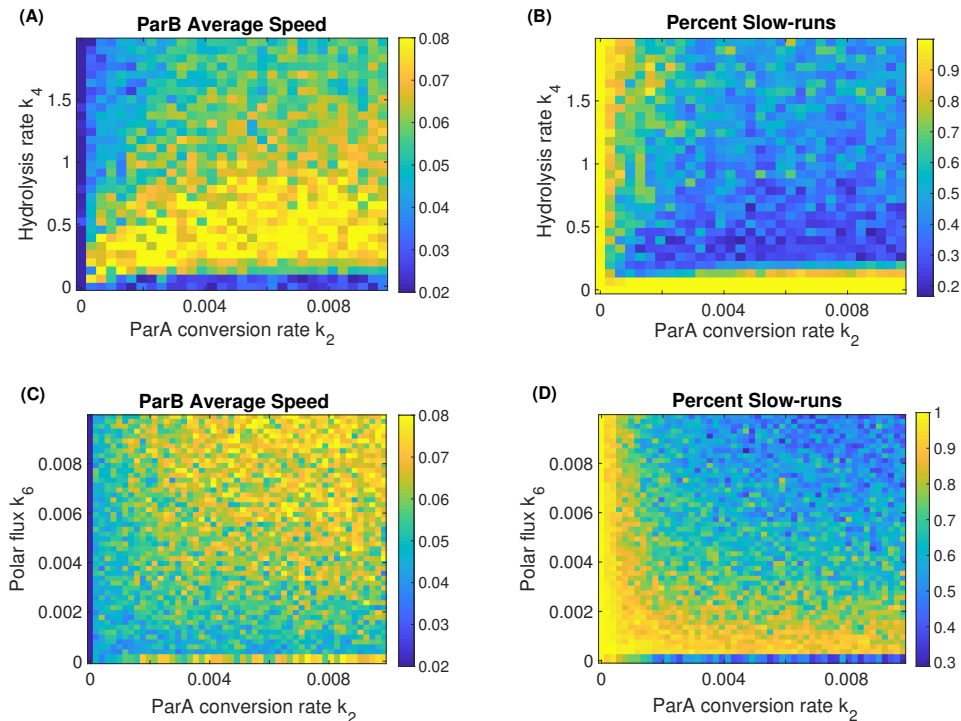
Figure 7: Two-parameter heat maps of ParB average speed and percentage of slow runs as function of k_2, k_4 and k_2, k_6 pairwise. (A) Heat map of ParB average speed as a function of k_2 and k_4. (B) Heat map of ParB slow run percentage as a function of k_2 and k_4. (C) Heat map of ParB's average speed as a function of k_2 and k_6. (D) Heat map of percentage of slow runs as a function of k_2 and k_6.

that faster ParA nucleoid binding can help overcome slow rate at which ParB-induced ParA ATP hydrolysis, thereby indicating a complementary role between these two reactions in improving ParB complex directed movement. We note Hu et al. (2017) reported similar patterns between ParB-induced hydrolysis rate and ParA binding rates; however, in our case we only see two modes of movement, namely directed and diffusive movement. Similarly, ParB experienced directed movement in the limits of high ParA nucleoid binding and high ParA polar sequestration, shown in Figure 7(C)-(D). Overall, the heatmaps highlight the nontrivial boundaries between directed and diffusive ParB motility modes as parameters are changed. We thus next seek to explore model response when multiple parameters are changed at the same time.

Global parameter sensitivity analysis.   Given the non-trivial relations between parameter values and model responses we sought to formally explore model response as multiple parameters are changed simultaneously. We focus our attention to a subset of parameters that showed non-trivial responses in the single parameter changes in the previous section. Specifically, we explore simultaneous variation of the following parameters: ParB diffusion coefficient (D_B), the rate ParB-induced ParA-ATP hydrolysis (k_4), ParA nucleoid binding rate (k_2) and polar PopZ sequestration rate (k_6) and keep the rest fixed.

 We employ two techniques reviewed by Marino et al. (2008), namely partial rank correlation coefficient (PRCC) and extended Fourier amplitude sensitivity test (eFAST) in order to rank the parameters in order of influence on mean velocities and percent slow runs. These techniques have wide spread use in various deterministic models, however they can be of significant use in computational stochastic models in cell biology where we have multiple parameters changing over wide ranges due to lack of direct measurement in experiments. Detailed implementation and discussion about these methods are beyond the scope of this paper, but they can be found in (Marino et al., 2008; Saltelli et al., 2008).

 Since a non-monotonic relationship between k_4 and the model outputs is present (as shown in the Figure 6), we split k_4 ranges into 2 intervals where monotonicity is preserved when we perform PRCC as follows. Low range k_4 includes all parameter combinations for which k_4 values are less than $0.1\,\text{s}^{-1}$, whereas $k_4 \geq 0.5\,\text{s}^{-1}$ are classified in the high k_4 range.

 Figure 8 shows the magnitude of PRCC values for each parameter of interest (D_B, k_4, k_2, k_6) with respect to the average speed and percentage of slow-runs corresponding to low and high range of k_4. In either low or high hydrolysis ranges, ParB speed and percentage of slow-runs remain consistently sensitive to k_4 and k_2 whereas the ranking of D_B and k_6 can change depending on k_4. In the low range, k_4 stands out as the most sensitive parameter and k_6 seems not to contribute into the average speed of ParB; however, in the high range of k_4, k_6 appears to be most sensitive with respect to both average speed and slow-runs percentage.
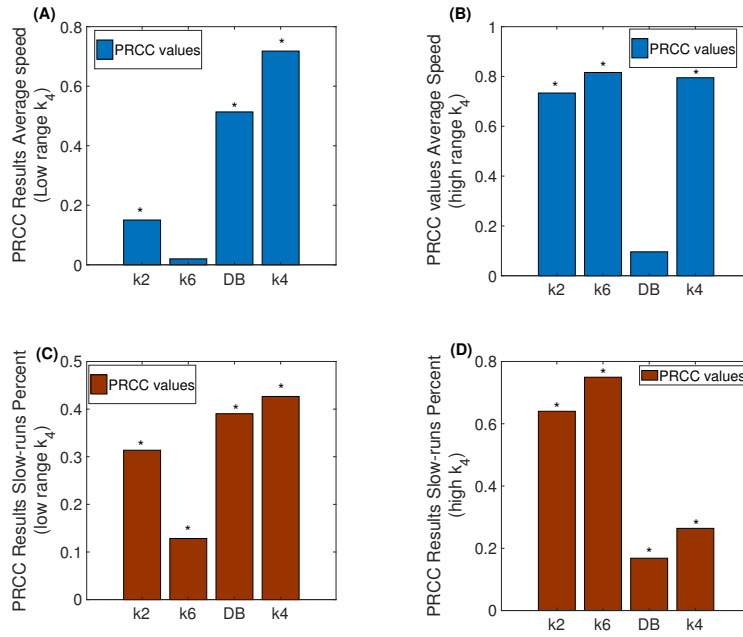
Figure 8: Bar plot of the magnitude of PRCC values for ParB complex average speed and short percent runs ($N = 500$) for low and high range of k_4. (A) PRCC of each parameter in the low range of k_4. (B) PRCC of each parameter in the high range of k_4. The symbol * marks statistical significance with $p < 0.01$.
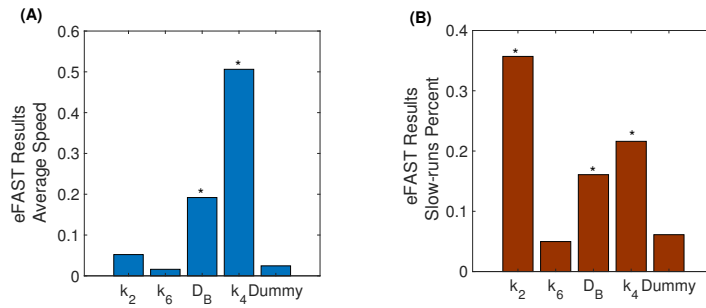
Figure 9: eFAST S_i index results ($N = 65$). (A) eFAST S_i results for average speed. (B) eFAST S_i results for slow-runs percent. The symbol * marks statistical significance ($p < 0.01$) measured using a Dummy variable.

Interestingly, we observe that the average speed and percentage of slow runs are both most sensitive to D_B in the low range of k_4 and in the high k_4 range they lose sensitivity to complex diffusion D_B with polar sequestration, k_6 becoming more important.

Next we examine eFAST ranking. There are two sensitivity measurements that are obtained through eFAST: 1) a first-order sensitivity index S_i, which represents the main contribution of an i th parameter to the overall model output variation and 2) a total sensitivity index S_{Ti}, which accounts for not only the main i th parameter contribution, but also captures the effects of its interaction with other parameters (Marino et al., 2008; Saltelli et al., 2008). Both S_i and S_{Ti} values range between 0 and 1. The smaller magnitude a sensitivity index is, the less influential it is to the model output variation. Ranking based on Si is typically suitable for linear models when the interactions among parameters do not contribute significantly to the output variance, while ranking based on S_{Ti} is more appropriate for nonlinear models. Here we consider both indexes. In addition, since the eFAST method can be applied when there are non-linear, non-monotonic relations between model parameters and model outputs, we do not need to split the parameter space here in subintervals as we did with PRCC.

The eFAST ranking displayed in Figure 9 shows that ParB speed and percent of slow runs are both sensitive to D_B and k_4 whereas percentage of slow-runs shows additional sensitivity to k_2 since both S_i and S_{Ti} remain significant for this parameter (see Table 2 for S_{Ti}). There is no conclusion on k_6 effects on speeds and percent slow runs using this ranking.

Table 2 combines all PRCC values and eFAST sensitivity indexes for each parameter for our two model outputs of ParB speed and percentage of slow runs. Since PRCC measures the correlation between the input parameters and the model outputs

Table 2: PRCC and eFAST summary. The order in which the parameters are listed reflects the magnitude of the sensitivity coefficient in absolute value from high to low (most sensitive to least sensitive).

Sensitivity Index	Parameters with significant sensitivity index	
	Speed	Percent
$eFAST - S_i$	k_4, D_B	k_2, k_4, D_B
$eFAST - S_{Ti}$	k_4, D_B	k_2, k_4
$PRCC$ (low k_4)	k_4, D_B, k_2	k_4, D_B, k_2, k_6
$PRCC$ (high k_4)	k_6, k_4, k_2	k_6, k_2, k_4, D_B
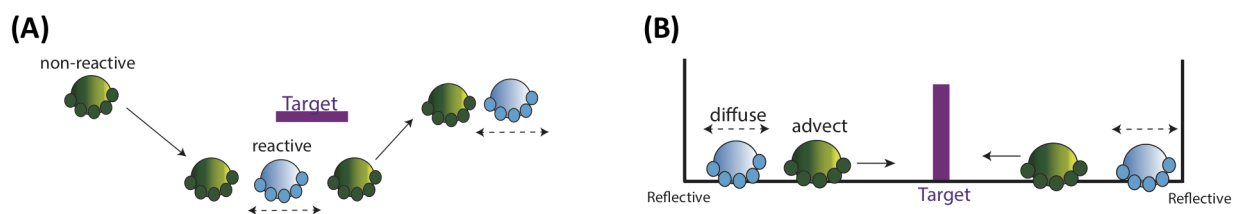
Figure 10: (A) Illustration of intermittent search strategies. Searcher (ParB) looks for a target. It alternates between fast relocation phases, which are not reactive (green) as they do not allow target detection and slow relocation phase, which are reactive (blue), allowing it to detect target (purple). (B) A minimal model of intermittent search for ParB. Periodic boundary condition is chosen as it is equivalent to the case of one target centered in a finite domain with reflective boundaries.

while eFAST measures the variance of the model under the effects of varying parameter values, their ranking may be different. However, in comparing their results, we note a common group of parameters that both methods agree as being critical to the model's outputs. So we highlight them here accordingly. The hydrolysis rate k_4 seems to be the most important parameter for both ParB average speed (also claimed by Hu et al., 2015) and percentage of slow runs. A second important parameter is the diffusion coefficient for ParB complexes, D_B which appears especially critical to average speeds under the low range of k_4 from our analysis. These results on k_4, D_B confirm the critical interplay of the rate ParB-induced ParA-ATP hydrolysis with ParB complex diffusion and can help explain prior work and our own simulation observations. In Figure 5 we saw that when k_4 is low, with a reduced diffusion coefficient $D_B = 0.0001\ \mu\text{m}^2\text{s}^{-1}$ as in the model of Lim et al. (2014) could lead ParB to fail to produce directed movement. Meanwhile, changing k_4 from a low $0.03\ \text{s}^{-1}$ to our baseline $0.5\ \text{s}^{-1}$ (the lower bound in the acceptable range for k_4 in Hu et al., 2015) can transition ParB from the reported diffusive movement of Lim et al. (2014) to directed movement as we observe here and in Hu et al. (2015). The role of low diffusion was questioned in (Hu et al., 2015, 2017); however, here we see that it is both the rate ParB-induced ParA-ATP hydrolysis rate and diffusion coefficient that can team up to prevent directed movement.

The rest of the parameters seem to show changes in ranking or statistical significance, however, the percentage of slow runs showed a consistent high ranking of k_2 in our analysis. This ranking makes sense since this parameter is responsible for the rate of ParA binding on the nucleoid and thus gradient formation, which is necessary in order to observe directed ParB movement as also reported by Hu et al. (2017).

3.2   A reduced intermittent search model for ParB movement

The local and global parameter sensitivity analysis in the previous section indicated that k_4, D_B, k_2, k_6 were important for ParB complex motility. Next, we explore a reduced model in the intermittent search framework (Bénichou et al., 2011; Newby and Bressloff, 2009) that only contained these key parameters and associated pathways for ParB complex motility, as assessed from the sensitivity analysis. This minimal modeling approach is novel and it allows us to more explicitly analyze ParB movement.

In this framework, the searcher (ParB) looks for a target (new pole) by alternating between fast directed ParA-bound state and a free diffusive (search) state. In the spirit of intermittent search models and in alignment with our simulations, ParB can only bind its target when it is in search state. So the question then is what is the best strategy for finding the target given that the complex can be in either a fast directed state or in a slow diffusive state. We explore this with a mean first passage approach next.

The ParB complex can be in either of the following 2 states within the interior of the cell:

- $n = 1$: diffusive state in which ParB diffuses along the one dimensional path.

- $n = 2$: advective state, during which it is inaccessible to react with any protein and moves with ballistic motion at a constant velocity v.

The target is assumed to be a perfect reactive point, that is the reaction occurs as soon as the target is reached by the protein and that ParB can only detect and bind to the target when it is in diffusive state. We further assume that ParA gradient is at steady state. We chose periodic boundary conditions as it is equivalent to the case of one target centered in a finite domain with reflective boundaries as illustrated in Figure 10(B) (Bénichou et al., 2011).

Let $p(x, i, t \mid x_0, i_0, t_0)$ be the probability that ParB at position x and state i at time t given that it initiated at position x_0, state i_0 at time t_0, which can be shortened as $p(x, i, t \mid x_0, i_0, 0) = p_i(x, t)$. Then $p_i(x, t)$ must satisfy the following forward Chapman-Kolmogorov equation:

$$\frac{\partial p_1}{\partial t} = D_B \frac{\partial^2 p_1}{\partial x^2} + k_4 p_2 - k_2 p_1$$
$$\frac{\partial p_2}{\partial t} = -v \frac{\partial p_2}{\partial x} - k_4 p_2 + k_2 p_1 \tag{1}$$

where we set $v = k_2 + k_6$. Note that this minimal model relies only on our knowledge of the key sensitive parameters k_4, D_B, k_6 and k_2. The motion of ParB in diffusive state ($n = 1$) is modeled by a continuous motion with diffusion coefficient D_B and k_4, k_2 are the transition rates between diffusive and advective state. When ParB detects ParA gradient, it advects with a constant speed v, which is assumed to be proportional to the total effect of k_2 and k_6.

Let $t(y, i)$ represent the average time needed for ParB to find the target given that it starts at some position y and in state i where $i = 1, 2$. It must satisfy the backward Chapman-Kolmogorov differential equations (Bénichou et al., 2005), which reads

$$D \frac{\partial^2 t(y, 1)}{\partial y^2} + k_4 [t(y, 2) - t(y, 1)] = -1,$$
$$v \frac{\partial t(y, 2)}{\partial y} + k_2 [t(y, 1) - t(y, 2)] = -1 \tag{2}$$

with boundary conditions:

$$t(0, 1) = t(L, 1) = 0$$
$$t(0, 2) = t(L, 2). \tag{3}$$

After some computations (see Supplementary Material, Section 4), we obtain the explicit average time solution:

$$t(y, 1) = \frac{k_4 + k_2}{k_4 k_2} \frac{L}{\beta - \alpha} \left[\beta^2 \frac{1 - e^{\alpha y}}{1 - e^{\alpha L}} - \alpha^2 \frac{1 - e^{\beta y}}{1 - e^{\beta L}} \right] - \frac{k_2 + k_4}{k_4} \frac{y}{v}$$

$$t(y, 2) = \frac{k_2 + k_4}{k_2 k_4} \frac{L}{\beta - \alpha} \left[\beta^2 \frac{1 - \frac{k_2}{v\beta} e^{\alpha y}}{1 - e^{\alpha L}} - \alpha^2 \frac{1 - \frac{k_2}{v\alpha} e^{\beta y}}{1 - e^{\beta L}} \right] - \frac{k_2 + k_4}{k_4} \frac{y}{v} - \frac{1}{k_4} \tag{4}$$

with $\alpha = \frac{1}{2} \left(\frac{k_2}{v} + \sqrt{\frac{k_2^2}{v^2} + 4\frac{k_4}{D}} \right)$ and $\beta = \frac{1}{2} \left(\frac{k_2}{v} - \sqrt{\frac{k_2^2}{v^2} + 4\frac{k_4}{D}} \right)$.

We next calculate ParB's average speed V given that it starts at the old pole $y = 0$ and at advective state $n = 2$ as $V = \frac{L}{t(0,2)}$. Since we are interested in the qualitative trend of the average arrival speed as a function of a single parameter while the rest is kept same as baseline values shown in Figure 11(D), we scale all the speeds in our results with their maximum value.

We note that most of the parameter values could be kept within the range of the values used for the computational model simulations with the exception of k_2 which had to be slightly varied; this is to be expected since this is only a minimal model and many other reactions have been omitted. However, the analytic velocity solution bears remarkably similar qualitative behavior as in the computational model simulations. In particular, in Figure 11(B), we see that the ParB velocities follow a non-monotonic growth trend with respect to the hydrolysis rate k_4 (compare with Figure 6(B)). This is in agreement with our computational model results and it supports our findings that there is an optimal hydrolysis rate that maximizes ParB velocities. In Figure 11(A)-(C) we also observe that as k_2 and D_B increase, ParB's average speed also increases and saturates quickly. These reduced model results are in agreement with our computational model simulations and indicate that an intermittent search formalism is an appropriate reduced modeling approach for this system.
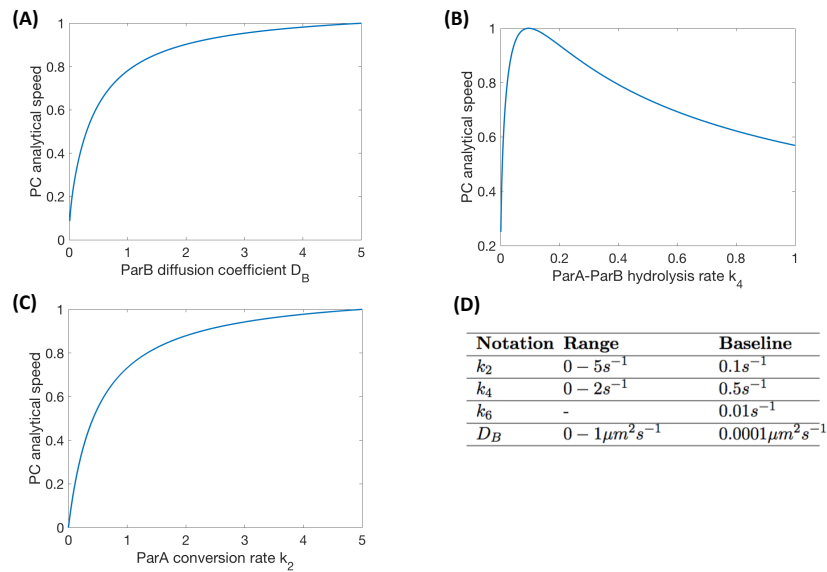
Figure 11: ParB average speed as a function of a single parameter using the reduced intermittent search model while the rest of the parameter are kept at fixed values listed in Table in panel (D). (A) ParB speed as a function of diffusion coefficient. (B) ParB speed as a function of hydrolysis rate k_4. (C) ParB speed as a function of ParA conversion rate k_2.

3.3   Establishment of bipolar MipZ concentrations

In this section, we return to the computational stochastic model. The new component here is that we add all MipZ reactions to ParA/ParB/PopZ reactions that were previously examined separately in Section 3.1. Our goal is to use the model to probe how the possibly competing relationship between ParA and MipZ for ParB binding sites could guide correct bipolar MipZ localization. Since the reactions are now quite complicated, we follow a step by step systematic procedure to evaluate how MipZ and ParA could be interacting with moving ParB complexes.

MipZ bipolar concentration with forced ParB binding saturation.   In previous experimental studies, MipZ bipolar concentration is established after ParB is anchored at the new pole for some time (Schofield et al., 2010). During this time ParA also accumulates preferentially at the new pole (Schofield et al., 2010), so we are interested in exploring how the interactions between ParB, ParA and MipZ might affect MipZ dynamics. Specifically, since MipZ and ParA both compete for the same binding sites on ParB it is possible that binding site competition can significantly affect MipZ accumulations. As a first step, we test this competition hypothesis by simulating our model without ParA and manually changing the total number of available ParB binding sites that MipZ can bind. Since MipZ gradient does not peak at the two poles until the mobile ParB copy is anchored, we also simulate our model by initializing with two anchored ParB complexes at each pole. This allows us to directly test the role of ParB binding sites on MipZ polar accumulations.

In Figure 12(A) we show averaged MipZ profiles along the long cell length (x-axis) in simulated cells (n = 50) without ParA and different numbers of ParB binding sites between an old pole associated and new pole associated ParB. To keep in line with experimental measurements, our computed profiles are averaged in time (250 time points) and then each time-averaged profile is averaged over 50 independent cell simulations. In Figure 12(B) we show two computed MipZ gradient quantities: mean MipZ midpoint position and MipZ peak ratio. On the x-axis we show the binding capacity ratio for ParB. A quadratic fit was applied to the time averaged MipZ profiles of each cell in order to estimate the minimum center position of a MipZ profile and then results were averaged over 50 trials to produce the mean MipZ midpoints. We record the minima as rescaled quantities by reporting the ratio between the distance from the minimum position to the old pole over total cell length. The MipZ distribution peak ratio was measured as the fraction between the new to old pole peaks of the fitting curve for each MipZ profile with a ratio of 1 indicating a perfectly symmetric distribution with two equal peaks. We plot the mean minimum positions and peak ratios against a binding capacity ratio which measures the available binding sites for MipZ at the new and old pole ParB respectively. For example, in Figure 12(B), 4:2 binding means that there are 4 binding sites available for MipZ at the old pole and there are 2 binding sites available for MipZ at the new pole ParB. In Figure 12(C) we show averaged MipZ profiles against cell length for both a wild-type cell (baseline parameters) and a mutant $\Delta tipN$ cell where there are equal amount of PopZ for both poles.

From the averaged profiles and computed midpoints and peak ratios in Figure 12(A)-(B), we observe the MipZ concentrations transitions from a symmetric to asymmetric conformation as the number of ParB binding sites becomes more different between
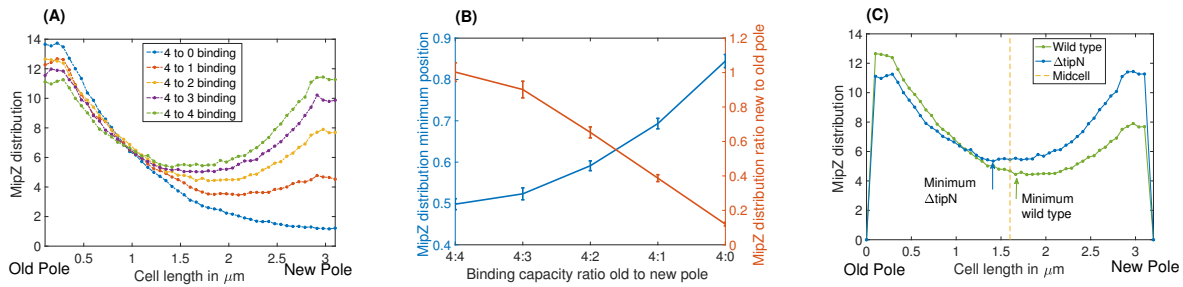
Figure 12: MipZ averaged profile in a cell without ParA. (A) Simulated average MipZ distributions ($n = 50$), fixing 4 binding sites at the old pole, varying at the new pole. (B) Error bar plot of the relative MipZ distribution minimum position (blue) and the ratio between 2 peaks (orange) as the function of the number of binding sites between ParB at the new and the old pole ($n = 50$). (C) Simulated average MipZ distribution ($n = 50$) in wild type (4 binding sites at the old pole and 3 at the new pole) and in $\Delta tipN$ (4 binding sites in both poles). All parameter values can be found from Table.1. Initially, there are 900 MipZ monomers.

the two ParB complexes. Specifically, as the binding capacity of ParB at the new pole decreases (i.e.,manual new pole ParB saturation), the minimum MipZ position in Figure 12(B) (blue curve) increases from 50% to close to 80%,(of the cell length) and the peak to peak ratio in MipZ concentration decreases from 100% to about 20%, Figure 12(B)(red curve). This indicates that MipZ gradient becomes more asymmetric as the new pole ParB becomes saturated.

In Figure 12(C) we simulated scenarios akin to the measurements in (Schofield et al., 2010) for averaged MipZ profiles of wild type vs $\Delta tipN$ mutant cells. TipN is a polar protein that has been shown to directly bind and interact with ParA monomers (Schofield et al., 2010) creating a condensed ParA accumulation at the new pole. It has also been observed that in $\Delta tipN$ cells, MipZ distribution along the cell has an average minimum position shifted toward the old pole while in wild type cells, the minima is biased toward the new pole. In our model, a $\Delta tipN$ cell is one that has equal binding potential for ParA between the two poles. From the average profiles in Figure 12(C), we observe a shift in minimum position from <49% to about 60% mark as the binding capacity in the new pole increases. Our results support a scenario in which the difference in MipZ distribution between wild type and $\Delta tipN$ mutant cell is due to the ratio between ParB binding capacity at the new pole versus the old pole. When both ParBs have the same binding capacity, MipZ distribution's average minimum position shifted toward the old pole. When this binding capacity at the new pole is less than in the old pole, MipZ's minimum position bias toward the new pole as seen in wild type cells. Our results are in full agreement with the data of Schofield et al. (2010).

Finally, we note that our model in this case explicitly tested ParB capacity by manually altering the number of binding sites in each anchored ParB, next we investigate whether ParA reactions are sufficient to mediate a transition between symmetric to asymmetric MipZ profiles by competing for ParB sites.

MipZ bipolar concentration with ParA saturation of ParB binding. Next, we re-introduce ParA in the cell in order to test whether the ParB binding site saturation we manually imposed before could be obtained through competition between ParA dimers and MipZ monomers. Similar to the previous set up we keep both ParBs anchored at the respective poles, but this time we keep them at the same binding capacity of four binding sites that can be occupied by either ParA or MipZ. We initialized the system with 300 ParA monomers and 900 MipZ monomers uniformly distributed along the cell. Since we have already observed that ParA gradient is affected by the imbalance of PopZ between the old and new pole, here we examined MipZ profiles for various numbers of PopZ at the new pole, while keeping the old pole fixed at 1 PopZ. We show average MipZ relative minimum position and peak-to-peak ratios in Figure 13(A).

When there is no PopZ at the new pole, the relative minimum MipZ position was below 50% and the peak-to-peak ratio was slightly greater than 1, Figure 13(A). As the PopZ ratio increases, the relative minimum position increases and it asymptotically approaches the mark of 60% of cell length. On the other hand, the peak to peak ratio decreases from an equal peak setup (peak ratio 1) to asymptotically approaching the asymmetric 0.6 peak ratio, Figure 13(A). We note the similarity between these results and the results in Figure 12(B) where the new pole binding sites were manually decreased; this indicates that the increasing of new pole accumulation of ParA also results in a fast saturation of ParB sites, which in turn can lower the access of MipZ to ParB binding sites. To test whether this saturation effect is the result of any differences between ParA binding affinity and MipZ binding affinity, in Figure 13(B) we recompute the mean MipZ peak positions and peak ratios as the values of ParB-MipZ reaction rate k_{11} are varied. We note that there is a wide range of k_{11} values that does not seem to affect the MipZ profiles, indicating that at the new pole ParA can dominate occupancy of ParB complex binding sites over a wide range of MipZ binding rates.
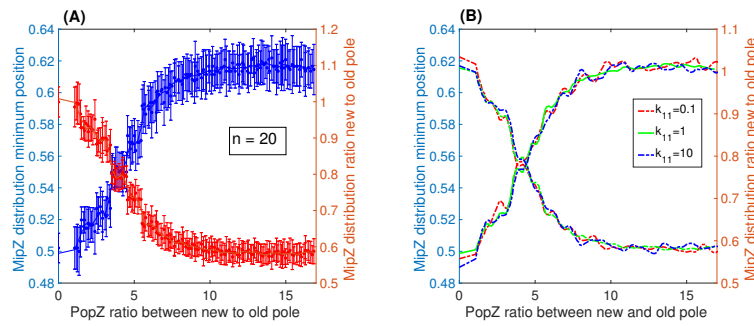
Figure 13: Simulated MipZ time average distribution ($n = 20$) in cells with ParA, varying the number of polar PopZ at the new pole and k_{11}. All parameter values can be found from Table 1 and the old pole is kept to have only 1 PopZ. (A) Plot of MipZ distribution relative minimum position (blue) and ratio between the two poles (red) when varying the number of polar PopZ at the new pole, $k_{11} = 1$ is used in this study. (B) Same as panel (A) for various values of $k_{11} = 0.1, 1, 10$.
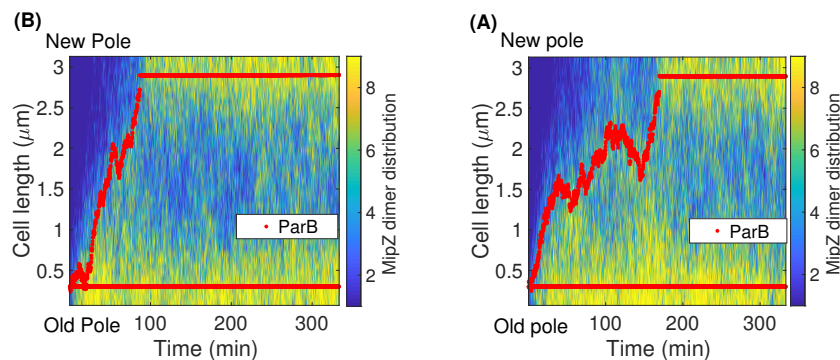
Figure 14: MipZ profile in a whole cell cycle including all the ParA proteins reactions. (A) Simulated ParB trajectory in wild type cell where there is 1 polar PopZ at the old pole and 20 polar PopZ at the new pole. (B) Simulated ParB trajectory in $\Delta tipN$ where there are 1 polar PopZ at each pole. All parameters can be found in Table 1, initially there are 300 ParA monomers and 900 MipZ monomers uniformly in the cell, 1 PopZ at the old pole and both ParBs are kept at the same binding capacity.

MipZ bipolar concentration formation in a full dividing cell model.   Finally, we revisit the full system including all the ParA proteins reactions in wild type and $\Delta tipN$ cell with all the MipZ reactions. Similar to the previous set up, we initialize the system with 300 ParA monomers and 900 MipZ monomers uniformly distributed along the cell. In this set-up, we allow both ParBs to start at the old pole, one of which is anchored and the other is free to move. They both are kept at the same binding capacity of only two binding sites that can be occupied by either ParA or MipZ (note that we lower the binding capacity here in the interest of reducing total simulation time).

2The kymographs in Figure 14 show ParB complexes and MipZ in a wild type and $\Delta tipN$ cell simulations. We note that ParB experienced less reversals in new-pole directed movement in wild type than in the $\Delta tipN$ cell, in agreement with data (Ptacin et al., 2010; Schofield et al., 2010).

3.3.1   Connecting MipZ gradient with FtsZ ring placement: a minimal model

The correct positioning of the division plane where FtsZ (or Z) ring polymerizes is a prerequisite for the generation of daughter cells in *Caulobacter*. Indeed, MipZ is the only known spatial regulator of FtsZ localization in *C. crescentus* (Sundararajan and Goley, 2017) as MipZ is hypothesized to directly interfere and restrict the formation of FtsZ ring until chromosome segregation has initiated. Furthermore, wild type cells show precise off center Z-ring localization (Schofield et al., 2010; Meier et al., 2017) with small fluctuations. From our MipZ simulations in this section, we also observed that the mean minimum MipZ concentration profile moved closer to mid-cell for $\Delta tipN$ mutants; we were curious whether at the single cell level it might be possible to detect differences in MipZ accumulation sufficiently in order to produce different Z-ring localizations in the case of wild type versus mutant cells.

2Since it is hypothesized that MipZ dimers directly inhibit FtsZ ring formation (Kiekebusch et al., 2012), here we explore how a simple MipZ repulsion model might affect FtsZ ring placement. For this purpose, we write a simple repulsion model,
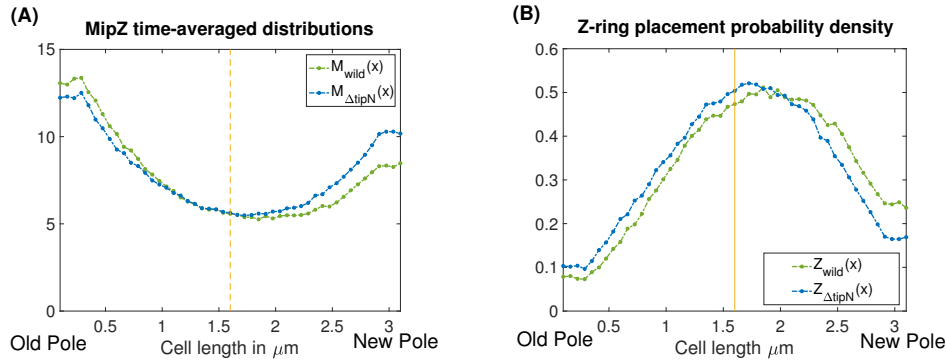
Figure 15: Z-ring placement probability density function derivation from the time average MipZ distribution in a single cell level in both wild type and $\Delta tipN$ cell. (A) Single cell simulation MipZ distribution in wild type (with 1 PopZ at the old pole and 20 PopZ at the new pole) and $\Delta tipN$ (with equal PopZ at both poles). (B) Probability density for the Z ring placement in wild type (green) and in $\Delta tipN$ (blue). All simulation parameters can be found in Table 1. Initially there are 300 ParA monomers and 900 MipZ monomers are placed uniformly in the cell and both ParBs are kept to have equal binding capacity.

where we postulate that the center of mass of the Z-ring is determined by minimizing an energy function that corresponds to MipZ profiles at any point in time, $M(x,t)$, which can be estimated by fitting our computational model results for MipZ dimer profiles. We write a Fokker-Planck equation for the probability density of finding the position of Z-ring center of mass x at time t, $Z(x,t)$ as follows,

$$\frac{\partial Z(x,t)}{\partial t} = -\frac{1}{\eta}\frac{\partial}{\partial x}[M'(x,t)Z(x,t)] + \frac{D_Z}{2}\frac{\partial^2}{\partial x^2}Z(x,t) \tag{5}$$

where $M'(x,t)$ denotes the derivative with respect to x and η is an affective drag coefficient for the ring. We assume that Z-ring diffuses with an effective coefficient D_Z and it advects proportional to MipZ concentration gradient. We did not explicitly estimate $M(x,t)$. Instead, we solve for the stationary solution of the above model with no flux boundary conditions at the two poles given by:

$$Z(x) = C\exp\left(\frac{M_i(x)}{k_B T}\right) \tag{6}$$

where k_B is the Boltzmann constant and C is a normalization constant. $M_i(x)$ is the time-average steady state concentration obtained from fitting a continuous function to our computational model results over 250 time points after both ParB are anchored at the two poles, shown in Figure 15(A) (indexed by model setup cases i = wild type, i = ΔtipN). We next compute the Z-ring positioning probability profiles for single cells both for wild type and $\Delta tipN$ cells in order to compare any potential consequences of the MipZ profile at the single cell level, which is where the decision for precise Z-ring placement must be made.

Figure 15(A) shows the time averaged MipZ profiles for a single wild type cell, $M_{wild}(x)$, and a $\Delta tipN$ cell, $M_{\Delta tipN}(x)$, which we then use to compute the FtsZ probability distributions in Figure 15(B). We note a significant overlap between wild type and $\Delta tipN$ Z-ring localization probabilities. This indicates that if we assume a simple MipZ repulsion model for FtsZ ring polymers, then the ring positioning could overlap in both wild type and $\Delta tipN$ mutants at the single cell level; thus potentially weaken the differences seen at the population level in Z-ring positioning based on observed MipZ concentration minima reported of Schofield et al. (2010). Furthermore, even at the single cell level we note that the MipZ concentrations tend to be rather shallow, thus likely to produce more diffuse Z-ring localization even when the MipZ concentration profile shows a minimum off the cell center- this observation stands in contrast to the narrow distribution of Z-ring positioning that Meier et al. (2017) observed in wild type *C. crescentus* cells. These results indicate that the relationship between MipZ and FtsZ ring components might be more complicated than simple repulsion and should be explored more closely.

4 Discussion

In this paper we have constructed a computational and minimal PDE models that use a gradient driven diffusion mechanism to generate persistent movement of a ParB partition complex in dividing *C. crescentus* cells. We first developed a detailed computational model that captured all relevant reactions. Our computational model includes some novel features that have not been examined before. First, we implemented detailed dimerization ParA reactions in conjunction with nucleoid and polar matrix binding in the cell. The inclusion of these reactions allowed us to test conditions for generation of directed movement of the ParB complex copy from the new to the old pole, as observed in experiments. Second, our computational model also

incorporated MipZ reactions and their interactions with the Par proteins; this allowed us to explore various conditions under which proper MipZ bipolar accumulation could occur both in wild type and mutant cells.

An important component of our computational model analysis was to apply global parameter sensitivity techniques in order to probe model response regimes using published parameter ranges. We were able to predict the parameter regions that produced different motility modes of the partition complex and ranked parameters in order of sensitivity. We found this approach to be important on two fronts. First, there is a wide range of parameters that appear in the modeling literature and various outcomes have been reported when using different parameter ranges so it is important to systematically explore parameter space. Second in the context of stochastic models in cell biology invariably a large set of parameters are needed in order to simulate so it is important that their effects are carefully studied besides presenting results that best match the available data, which many times can be limited.

From our parameter sensitivity analysis we found the ParB-induced hydrolysis rate of ParA, k_4, to be of critical sensitivity in the context of generating directed ParB movement. The reason for this is that although ParA gradient can provide significant guidance to a partition complex, low hydrolysis rates increase the time it takes for ParB to release ParA off the nucleoid thereby weakening the ability of the complex to read variations in local concentrations of ParA. Indeed, in the model (Lim et al., 2014) ParB complexes were unable to generate sustained directed movement despite an effective gradient condition imposed on ParA; our model could recoup similar behavior in ranges of low rate of ParA hydrolysis. We note that in (Lim et al., 2014) the observed lack of directionality was the impetus for proposing that elastic DNA connections were necessary in order to generate ParB movement. Our model instead indicates that diffusion can be sufficient to move ParB up a new pole-generated ParA gradient within a wide range of parameter values. Indeed, other diffusion driven models such as the one from Hu et al. (2015, 2017) have proposed similar mechanisms, however in their treatment both cell geometry and ParA reactions were not included. In addition to hydrolysis rates, the value of ParB diffusion coefficients seems to affect differences in model outcomes for Lim et al. (2014) versus Hu et al. (2015, 2017). In our analysis we found that low diffusion coefficient rank as high sensitivity only when the rates ParB-induced ParA-ATP hydrolysis are slow and are otherwise not as important if ParB is efficient at burning ATP and thus reading the ParA gradient. These results are in agreement with a mechanism for which movement directionality for ParB can be thought as the result of a combination of efficient ParA hydrolysis with a sufficient new pole directed gradient. Overall, we find that systematic parameter explorations can be of tremendous help when testing model behaviors at the sub-cellular scale.

Although the computational model provided a comprehensive reaction network including ParA, ParB, PopZ, MipZ, it is rather complex and computationally expensive to simulate. Combining the insight from the computational model results and the parameter sensitivity analysis, we were able to construct a minimal intermittent-search model (Bénichou et al., 2005, 2011), which relied on only four most sensitive parameters for predicting ParB motility. We could fully solve this model analytically and we showed that this reduced formulation may be the simplest model that can capture the complex dynamics of ParB movement toward the new pole in the presence of ParA clouds. We anticipate that this framework could be a productive approach in this setting and that might be worth exploring further for more complicated cellular setups (for example including cases in which ParB experiences bidirectional movement that depends more explicitly on ParA concentrations).

We also used the computational model to probe the ability of polar PopZ complexes to affect partition complex segregation through interactions with cytoplasmic ParA monomers. We observed sporadic ParB complex movement reversals when adjusting the number of polar PopZ at the two poles and the number of ParA in the cell. In our model, PopZ polar protein numbers can be adjusted to incorporate new pole landmark protein TipN effects in the cell. In simulated $\Delta tipN$ cells with overproduction of ParA, ParB complexes experienced loss of directionality and frequent direction reversals in agreement with experiments of Schofield et al. (2010); however, in contrast to experimental observations we did not observe oscillatory ParA localization and ParB movement between the two poles in conditions of significant ParA overexpression, as has sometimes been observed in experimental conditions (Schofield et al., 2010). This finding stands in agreement with results of Shtylla (2017) where oscillatory ParB regimes were only observed in the presence of cytoplasmic PopZ complexes; cytoplasmic PopZ complexes were proposed as an important factor in segregation by Laloux and Jacobs-Wagner (2013), however their reaction dynamics with ParA are still not well understood and as such were not included in our model. Taken together these findings indicate that polar saturation is not sufficient to generate oscillatory patterns in *C. crescentus* cells. We also observed that even in conditions of ParA overexpression, slight differences in PopZ protein concentrations at each pole were sufficient to produce some directed movement of ParB complexes, indicating that even weak polar gradient of ParA can be sufficient to guide a ParB complex to a pole. Overall our results are in agreement with data of Schofield et al. (2010) and Ptacin et al. (2010, 2014) that indicate that a new pole directed gradient generated by increased ParA monomer capture and re-dimerization at the new pole in the presence of PopZ and TipN is sufficient generate directed ParB movement.

Our computational model was also used to explore the interactions between MipZ and Par proteins in order to get insight into how MipZ bipolar concentrations are formed and coordinated with chromosome segregation. MipZ gradient are a central signaling component for proper FtsZ ring placement at the cell division plane in *C. crescentus*. Our results indicate that competition for limited binding sites on ParB complexes is sufficient to generate asymmetric MipZ bipolar distributions with midpoints closer to the new pole. This asymmetry is achieved thanks to preferential accumulation of ParA at the new pole which in turn

competes for ParB binding sites as the ParB complex translocates to the new pole. Our simulations also showed that increasing PopZ protein presence at the new pole led to higher numbers of ParA dimers the new pole created more asymmetric MipZ concentration profiles with the relative minimum position biased toward the new pole.

Finally, we examined using a reduced PDE model whether MipZ concentrations at the single cell level were sufficient to control Z-ring localization. MipZ is the only known spatial regulator of Z ring formation due to its inhibitory reaction to FtsZ ring components. Our results show that the simulated MipZ concentration in wild type is rather shallow and thus likely to produce diffuse Z-ring localization which stands in contrast to the narrow distribution of Z-ring reported by Meier et al. (2017). Our results also showed a significant overlap in Z-ring localization probabilities between wild type and mutant cells. Taken together, our results indicate that a simple MipZ profile signal may be insufficient to control Z-ring placement near the middle of the cell. Thus, we suggest that there may be other mechanisms in *C. crescentus* beside MipZ bipolar concentration that enhance the precision in Z-ring placement during the cell division that should be explored more closely.

In conclusion, we have constructed models that incorporated ParA, ParB, PopZ and MipZ dynamics in order to explore the asymmetric division events in *C. crescentus*. Our model results are in agreement with various experimental observations and the modeling framework can be used to probe various proposed mechanisms that affect cell division. While we were able to incorporate many known mechanisms in our model, there are of course a series of items that could be further incorporated particularly once more data becomes available. First, we did not incorporate potential elastic connections between ParB and ParA, mainly in interest of simplicity since our focus was on creating a framework in which both chromosome segregation and division plate placement reactions could be studied together. We note however, that our results are in line with a diffusion driven mechanism proposed by Hu et al. (2015, 2017) and our results agree despite the lack of detailed elastic connection modeling for ParB. In addition, much more work remains in the elucidation of the role of cytoplasmic PopZ, and more detailed interactions between FtsZ components and MipZ and how these interactions result in precise positioning of the Z-ring. These are issues that we intend to pursue in future work.

Acknowledgments

References

Andrews, S. S. (2016). Smoldyn: particle-based simulation with rule-based modeling, improved molecular interaction and a library interface. *Bioinformatics 33*(5), 710–717. 195

Andrews, S. S., N. J. Addy, R. Brent, and A. P. Arkin (2010). Detailed simulations of cell biology with smoldyn 2.1. *PLoS computational biology 6*(3), e1000705. 195, 196

Andrews, S. S. and D. Bray (2004). Stochastic simulation of chemical reactions with spatial resolution and single molecule detail. *Physical biology 1*(3), 137. 195, 196

Banigan, E. J., M. a. Gelbart, Z. Gitai, N. S. Wingreen, and A. J. Liu (2011, September). Filament depolymerization can explain chromosome pulling during bacterial mitosis. *PLoS computational biology 7*(9), e1002145. 192

Bénichou, O., M. Coppey, M. Moreau, P. Suet, and R. Voituriez (2005). Optimal search strategies for hidden targets. *Physical review letters 94*(19), 198101. 205, 210

Bénichou, O., C. Loverdo, M. Moreau, and R. Voituriez (2011). Intermittent search strategies. *Reviews of Modern Physics 83*(1), 81. 192, 204, 205, 210

Blinov, M. L., J. R. Faeder, B. Goldstein, and W. S. Hlavacek (2004). Bionetgen: software for rule-based modeling of signal transduction based on the interactions of molecular domains. *Bioinformatics 20*(17), 3289–3291. 195

Bonny, M., E. Fischer-Friedrich, M. Loose, P. Schwille, and K. Kruse (2013, December). Membrane binding of MinE allows for a comprehensive description of Min-protein pattern formation. *PLoS computational biology 9*(12), e1003347. 198

Bowman, G. R., L. R. Comolli, G. M. Gaietta, M. Fero, S.-H. Hong, Y. Jones, J. H. Lee, K. H. Downing, M. H. Ellisman, H. H. McAdams, et al. (2010). Caulobacter popz forms a polar subdomain dictating sequential changes in pole composition and function. *Molecular microbiology 76*(1), 173–189. 191

Bowman, G. R., L. R. Comolli, J. Zhu, M. Eckart, M. Koenig, K. H. Downing, W. E. Moerner, T. Earnest, and L. Shapiro (2008, Sep). A polymeric protein anchors the chromosomal origin/parb complex at a bacterial cell pole. *Cell 134*(6), 945–955. 191, 194

Easter Jr, J. and J. W. Gober (2002). Parb-stimulated nucleotide exchange regulates a switch in functionally distinct para activities. *Molecular cell 10*(2), 427–434. 191

Ebersbach, G., A. Briegel, G. J. Jensen, and C. Jacobs-Wagner (2008). A self-associating protein critical for chromosome attachment, division, and polar organization in caulobacter. *Cell 134*(6), 956–968. 191

Elowitz, M. B., M. G. Surette, P.-E. Wolf, J. B. Stock, and S. Leibler (1999). Protein mobility in the cytoplasm ofescherichia coli. *Journal of bacteriology 181*(1), 197–203. 198

Figge, R. M., A. V. Divakaruni, and J. W. Gober (2004). Mreb, the cell shape-determining bacterial actin homologue, co-ordinates cell wall morphogenesis in caulobacter crescentus. *Molecular microbiology 51*(5), 1321–1332. 191

Hu, L., A. G. Vecchiarelli, K. Mizuuchi, K. C. Neuman, and J. Liu (2015). Directed and persistent movement arises from mechanochemistry of the para/parb system. *Proceedings of the National Academy of Sciences 112*(51), E7055–E7064. 192, 198, 200, 204, 210, 211

Hu, L., A. G. Vecchiarelli, K. Mizuuchi, K. C. Neuman, and J. Liu (2017). Brownian ratchet mechanism for faithful segregation of low-copy-number plasmids. *Biophysical journal 112*(7), 1489–1502. 192, 198, 200, 202, 204, 210, 211

Hwang, L. C., A. G. Vecchiarelli, Y.-W. Han, M. Mizuuchi, Y. Harada, B. E. Funnell, and K. Mizuuchi (2013, May). ParA-mediated plasmid partition driven by protein pattern self-organization. *The EMBO journal 32*(9), 1238–49. 192, 194

Kiekebusch, D., K. A. Michie, L.-O. Essen, J. Löwe, and M. Thanbichler (2012). Localized dimerization and nucleoid binding drive gradient formation by the bacterial cell division inhibitor mipz. *Molecular cell 46*(3), 245–259. 192, 194, 198, 208

Kiekebusch, D. and M. Thanbichler (2014, February). Spatiotemporal organization of microbial cells by protein concentration gradients. *Trends in microbiology 22*(2), 65–73. 191, 192

Laloux, G. and C. Jacobs-Wagner (2013, June). Spatiotemporal control of PopZ localization through cell cycle-coupled multi-merization. *The Journal of cell biology 201*(6), 827–41. 194, 210

Laloux, G. and C. Jacobs-Wagner (2014). How do bacteria localize proteins to the cell pole? *Journal of cell science 127*(1), 11–19. 198

Li, F., K. Subramanian, M. Chen, J. J. Tyson, and Y. Cao (2016). A stochastic spatiotemporal model of a response-regulator network in the caulobacter crescentus cell cycle. *Physical biology 13*(3), 035007. 192

Li, S., P. Brazhnik, B. Sobral, and J. J. Tyson (2009). Temporal controls of the asymmetric cell division cycle in caulobacter crescentus. *PLoS Comput Biol 5*(8), e1000463. 192

Lim, H., I. Surovtsev, B. Beltran, F. Huang, J. Bewersdorf, and C. Jacobs-Wagner (2014). Evidence for a DNA-relay mechanism in ParABS-mediated chromosome segregation. *eLife 2014*(3). 191, 192, 195, 197, 198, 199, 200, 204, 210

Lipkow, K., S. S. Andrews, and D. Bray (2005). Simulated diffusion of phosphorylated chey through the cytoplasm of escherichia coli. *Journal of bacteriology 187*(1), 45–53. 195

Marino, S., I. B. Hogue, C. J. Ray, and D. E. Kirschner (2008). A methodology for performing global uncertainty and sensitivity analysis in systems biology. *Journal of theoretical biology 254*(1), 178–196. 202, 203

Meier, E. L., A. K. Daitch, Q. Yao, A. Bhargava, G. J. Jensen, and E. D. Goley (2017). Ftsex-mediated regulation of the final stages of cell division reveals morphogenetic plasticity in caulobacter crescentus. *PLoS genetics 13*(9), e1006999. 208, 209, 211

Mohl, D. A., J. Easter, and J. W. Gober. The chromosome partitioning protein, parb, is required for cytokinesis in caulobacter crescentus. *Molecular Microbiology 42*(3), 741–755. 194

Mohl, D. a. and J. W. Gober (1997, March). Cell cycle-dependent polar localization of chromosome partitioning proteins in Caulobacter crescentus. *Cell 88*(5), 675–84. 191, 194

Newby, J. M. and P. C. Bressloff (2009). Directed intermittent search for a hidden target on a dendritic tree. *Physical Review E 80*(2), 021913. 204

Ptacin, J. L., A. Gahlmann, G. R. Bowman, A. M. Perez, A. R. S. von Diezmann, M. R. Eckart, W. E. Moerner, and L. Shapiro (2014, May). Bacterial scaffold directs pole-specific centromere segregation. *Proceedings of the National Academy of Sciences of the United States of America 111*, E2046–E2055. 191, 194, 210

Ptacin, J. L., S. F. Lee, E. C. Garner, E. Toro, M. Eckart, L. R. Comolli, W. E. Moerner, and L. Shapiro (2010, August). A spindle-like apparatus guides bacterial chromosome segregation. *Nature cell biology 12*(8), 791–8. 191, 192, 194, 208, 210

Quardokus, E. M. and Y. V. Brun (2002). Dna replication initiation is required for mid-cell positioning of ftsz rings in caulobacter crescentus. *Molecular microbiology 45*(3), 605–616. 191

Saltelli, A., M. Ratto, T. Andres, F. Campolongo, J. Cariboni, D. Gatelli, M. Saisana, and S. Tarantola (2008). *Global sensitivity analysis: the primer*. John Wiley & Sons. 202, 203

Schofield, W. B., H. C. Lim, and C. Jacobs-Wagner (2010). Cell cycle coordination and regulation of bacterial chromosome segregation dynamics by polarly localized proteins. *The EMBO Journal 29*(18), 3068–3081. 191, 194, 199, 206, 207, 208, 209, 210

Shebelut, C. W., J. M. Guberman, S. Van Teeffelen, A. A. Yakhnina, and Z. Gitai (2010). Caulobacter chromosome segregation is an ordered multistep process. *Proceedings of the National Academy of Sciences 107*(32), 14194–14198. 191

Shtylla, B. (2017). Mathematical modeling of spatiotemporal protein localization patterns in c. crescentus bacteria: A mechanism for asymmetric ftsz ring positioning. *Journal of theoretical biology 433*, 8–20. 192, 195, 198, 199, 210

Shtylla, B. and J. P. Keener (2012, August). A mathematical model of para filament-mediated chromosome movement in caulobacter crescentus. *Journal of theoretical biology 307*, 82–95. 192

Shtylla, B. and J. P. Keener (2015). Mathematical modeling of bacterial track-altering motors: Track cleaving through burnt-bridge ratchets. *Physical Review E 91*(4), 042711. 192, 198

Sliusarenko, O., J. Heinritz, T. Emonet, and C. Jacobs-Wagner (2011, May). High-throughput, subpixel precision analysis of bacterial morphogenesis and intracellular spatio-temporal dynamics. *Molecular microbiology 80*(3), 612–27. 198

Sundararajan, K. and E. D. Goley (2017). Cytoskeletal proteins in caulobacter crescentus: Spatial orchestrators of cell cycle progression, development, and cell shape. In *Prokaryotic Cytoskeletons*, pp. 103–137. Springer. 191, 192, 208

Surovtsev, I. V., M. Campos, and C. Jacobs-Wagner (2016). Dna-relay mechanism is sufficient to explain para-dependent intracellular transport and patterning of single and multiple cargos. *Proceedings of the National Academy of Sciences 113*(46), E7268–E7276. 191, 198

Surovtsev, I. V., H. C. Lim, and C. Jacobs-Wagner (2016, Jun). The slow mobility of the para partitioning protein underlies its steady-state patterning in caulobacter. *Biophysical journal 110*, 2790–2799. 192, 198

Thanbichler, M. and L. Shapiro (2006). Mipz, a spatial regulator coordinating chromosome segregation with cell division in caulobacter. *Cell 126*(1), 147–162. 192, 194

Thanbichler, M. and L. Shapiro (2008, January). Getting organized–how bacterial cells move proteins and DNA. *Nature reviews. Microbiology 6*(1), 28–40. 191

Toro, E., S.-H. Hong, H. H. McAdams, and L. Shapiro (2008). Caulobacter requires a dedicated mechanism to initiate chromosome segregation. *Proceedings of the National Academy of Sciences 105*(40), 15435–15440. 191, 194

Vecchiarelli, A. G., Y.-W. Han, X. Tan, M. Mizuuchi, R. Ghirlando, C. Biertümpfel, B. E. Funnell, and K. Mizuuchi (2010, October). ATP control of dynamic P1 ParA-DNA interactions: a key role for the nucleoid in plasmid partition. *Molecular microbiology 78*(1), 78–91. 194, 198

Vecchiarelli, A. G., K. Mizuuchi, and B. E. Funnell (2012, November). Surfing biological surfaces: exploiting the nucleoid for partition and transport in bacteria. *Molecular microbiology 86*(3), 513–23. 192, 194

Vecchiarelli, A. G., K. C. Neuman, and K. Mizuuchi (2014, April). A propagating ATPase gradient drives transport of surface-confined cellular cargo. *Proceedings of the National Academy of Sciences of the United States of America 111*(13), 4880–5. 192, 198

Weber, S. C., A. J. Spakowitz, and J. A. Theriot (2010, Jun). Bacterial chromosomal loci move subdiffusively through a viscoelastic cytoplasm. *Physical review letters 104*, 238102. 198